Materials & Design 264 (2026) 115768

Contents lists available at ScienceDirect

Materials & Design

journal homepage: www.elsevier.com/locate/matdes

The effects of recrystallisation on the fatigue and corrosion properties of LB-PBF stainless steel 316L☆

Charlie Bevan [a], Thomas Jones [b], Amar Malla [c], James Sullivan [c], David Penney [c], Robert Lancaster [a,*]

[a] Institute of Structural Materials, Bay Campus, Swansea University, Swansea SA1 8EN, UK
[b] Rolls-Royce Plc, PO Box 2000, Derbyshire DE24 7XX, UK
[c] Faculty of Science & Engineering, Bay Campus, Swansea University, Swansea SA1 8EN, UK

ARTICLE INFO

Keywords:
Stainless steel 316L
Laser beam powder bed fusion
Recrystallisation
Mechanical properties
Corrosion resistance

ABSTRACT

This study investigates the influence of post-build heat treatments (HTs) on the microstructural evolution, mechanical performance, and corrosion resistance of laser beam powder bed fusion (LB-PBF) stainless steel 316 L. Samples built in vertical and horizontal orientations were subjected to three HT conditions (1050, 1150, and 1200 °C), enabling analysis of recrystallisation behaviour, grain morphology, and the mitigation of anisotropy. Tensile, low-cycle fatigue (LCF), and fatigue crack growth (FCG) testing revealed that full recrystallisation occurred at ≥ 1150 °C, reducing orientation-dependent discrepancies in strength and ductility. Despite improved isotropy, LCF testing demonstrated residual anisotropy, with samples built in the vertical orientation consistently outperforming those built in the horizontal orientation. Samples heat treated at 1050 °C retained a fine, columnar grain structure, resulting in superior resistance to crack growth due to increased yield strength and grain boundary density. In contrast, samples heat treated at 1150 and 1200 °C exhibited coarser, equiaxed grains with diminished fatigue crack resistance. Cyclic polarisation testing showed recrystallisation at the higher temperatures induced positive changes in corrosion performance, substantially increasing pitting potential compared to un-recrystallised microstructures, as found at 1050 °C. The findings highlight the trade-offs between strength, ductility, and fatigue resistance as a function of microstructure, offering insight into optimising HT protocols for LB-PBF SS316L components in fatigue-critical applications.

1. Introduction

Laser beam powder bed fusion (LB-PBF) is an additive manufacturing (AM) technique that fabricates components layer by layer using a high-powered laser to selectively melt and fuse layers of metallic powder. A digital 3D model is sliced into a series of two-dimensional cross-sections, which the laser traces sequentially to build up the final part [1]. As the laser interacts with the powder bed, it generates melt pools that partially remelt previously solidified material, producing a distinctive columnar microstructure shaped by overlapping melt pools and steep thermal gradients [2,3]. The morphology and distribution of these microstructural features are highly sensitive to process parameters such as laser power, scan speed, hatch spacing, and layer thickness. Careful control and optimisation of these settings are essential for achieving near-full density and desirable mechanical performance.

One of the primary challenges in LB-PBF lies in managing the variability in mechanical properties, which arises from the complex thermal history and inherent microstructural anisotropy [4] of the process. Steep temperature gradients and rapid solidification promote epitaxial grain growth, resulting in directional microstructures that are strongly dependent on build orientation. Moreover, the process is susceptible to defects such as lack of fusion (LoF), gas porosity, and surface roughness. These imperfections are particularly detrimental under cyclic loading conditions, where fatigue performance is more sensitive to microstructural inconsistencies than tensile properties. Consequently, while LB-PBF components can achieve tensile strengths comparable to or exceeding those of conventionally manufactured parts, they often exhibit reduced fatigue resistance due to these process-related flaws.

Among the materials processed using LB-PBF, stainless steel 316 L (SS316L) is widely used due to its excellent printability, corrosion

☆ This article is part of a special issue entitled: 'Additive Manufacturing' published in Materials & Design.

* Corresponding author.
E-mail address: r.j.lancaster@swansea.ac.uk (R. Lancaster).

https://doi.org/10.1016/j.matdes.2026.115768
Received 19 December 2025; Received in revised form 2 February 2026; Accepted 27 February 2026
Available online 3 March 2026

resistance, and mechanical performance, making it a strong candidate for applications in the aerospace and marine industries [5,6]. The as-built microstructure of LB-PBF SS316L typically consists of fine solidification cells within a face-centered cubic (FCC) austenitic matrix [7]. Due to the nature of the layer-wise thermal cycles, the resulting microstructure is inherently anisotropic, driven by the steep and repetitive thermal gradients during fabrication [3–9]. Epitaxial grain growth is commonly observed, with grains traversing multiple melt pool boundaries and aligning predominantly along the build direction.

The LB-PBF process is influenced by a range of parameters, including powder characteristics, processing conditions, and build orientation. Each of these factors can contribute to variability in the final component's microstructure and mechanical properties. To mitigate this, post manufacture processing such as heat treatments (HT) and hot isostatic pressing (HIP) [10] are a common approach used to improve the reliability and structural integrity of metallic materials built via LB-PBF. Whereas HIP is primarily designed to close any residual porosity, the process can also promote favourable microstructural changes such as recrystallisation, akin to HT regimes [11]–[12]. However, while such post-processing routes can enhance ductility, corrosion resistance, and property consistency, they may also compromise attributes such as strength or fatigue crack resistance, highlighting the need for careful optimisation.

In conventionally processed SS316L, the understanding of appropriate heat treatments is well established, with solution annealing typically performed in the range of approximately 1040–1120 °C, followed by rapid cooling to dissolve secondary phases and restore corrosion resistance [13,14]. In contrast, the response of LB-PBF SS316L to thermal exposure is more complex due to its non-equilibrium microstructure, high dislocation density, strong crystallographic texture, and the presence of fine oxide inclusions introduced during processing [15–17]. These features enable a high as-built strength but also influence recovery and recrystallisation behaviour, often resulting in recrystallisation kinetics that differ markedly from those observed in wrought material.

Recent studies have shown that recrystallisation in LB-PBF SS316L is frequently governed by strain-induced boundary migration (SIBM) rather than classical nucleation and growth, with grain boundary mobility strongly affected by Zener pinning from finely dispersed oxide particles [18]. At elevated temperatures and extended hold times, coarsening of these inclusions can reduce pinning efficiency, enabling accelerated boundary migration, recrystallisation, and subsequent grain growth [18].

As a result, a wide range of heat-treatment strategies has been reported for LB-PBF SS316L, spanning low-temperature stress-relief treatments aimed at reducing residual stresses while retaining as-built strength, through to high-temperature annealing or solutionising treatments designed to promote microstructural homogenisation and improved isotropy processing [15–17]. Despite this growing body of work, there remains no consensus on an optimal heat-treatment window, particularly for fatigue-critical applications, as improvements in isotropy and corrosion behaviour can be accompanied by reductions in strength or crack-growth resistance [15–17]. This highlights the need to systematically link recrystallisation behaviour with mechanical and environmental performance.

In this context, the present study focuses on three discrete high-temperature HT regimes at 1050, 1150, and 1200 °C. The temperature of 1050 °C lies at the lower bound of conventional solution annealing and is expected to promote recovery while largely preserving the as-built microstructure. The intermediate temperature of 1150 °C was selected to activate recrystallisation mechanisms without excessive grain growth, providing insight into the transition between recovery-dominated and fully recrystallised states. Finally, 1200 °C represents an upper-bound annealing condition, where full recrystallisation and grain growth are anticipated, enabling assessment of the performance trade-offs associated with extensive microstructural homogenisation. This study comprehensively investigates the effects of these HT conditions on the microstructure, low cycle fatigue (LCF), fatigue crack growth (FCG) behaviour, and corrosion resistance of LB-PBF fabricated SS316L. A particular focus is placed on understanding how build orientation and subsequent recrystallisation influence the fully reversed fatigue performance of the alloy.

An extensive and systematic fatigue testing programme was conducted on laboratory-scale specimens produced in two build orientations: namely, vertical (or normal to the powder bed, 90°) and horizontal (or parallel to the powder bed, 0°). The influence of HT on the mechanical response under cyclic loading was evaluated by examining changes in fatigue life and crack propagation characteristics across different HT processing conditions. In addition to mechanical testing, detailed microstructural and fractographic analyses were performed to correlate fatigue behaviour with underlying material features. These characterisations aim to assess the sensitivity of LB-PBF SS316L to various HT conditions, with an emphasis on the potential for enhanced microstructural homogenisation between the two build orientations. Ultimately, the goal is to reduce the fatigue life discrepancies commonly observed between differently oriented specimens, understand the differences in corrosion behaviour and to provide guidance for optimising post-processing routes to improve the reliability and performance of LB-PBF SS316L components in cyclic service environments.

2. Materials and experimental methods

2.1. Materials & samples

In this study, a series of vertical (90°) and horizontal (0°) cylindrical and octagonal blanks were manufactured using virgin SS316L powder at Rolls Royce Submarines Ltd (RRSL). Both the powder particle size distribution (PSD) and the chemistry was analysed prior to specimen manufacture. The corresponding elemental composition and PSD are presented in Tables 1 and 2.

The components were built on an EOS M290 LB-PBF machine using industry standard LB-PBF parameters for SS316L with a powder size distribution ranging from 10-49 μm, each of which were built with an equivalent energy density of 100 J/mm^3 and a layer thickness of 20 μm. The selected total energy density (E) was calculated using the following equation:

$$E = \frac{P}{v.h.t} \tag{1}$$

Where: E = energy density (J/mm^3), P = laser power (W), v = laser scanning speed (mm/s), h = hatch spacing (mm) and t = layer thickness (mm).

Two specimen batches were produced corresponding to the mechanical test types and designed to cover both vertical and horizontal build orientations, as well as multiple heat treatments. Since all specimens were fabricated on a single build plate, variables including powder characteristics and build-to-build variations were minimised. This uniformity ensures that differences in fatigue life can be predominantly related to the unique microstructures produced by each heat treatment. These specimens were subsequently used for fatigue crack growth and uniaxial tensile testing (Fig. 1a & b) and low cycle fatigue (Fig. 1c & d) testing. To provide a comparative baseline for microstructural and mechanical properties, conventionally wrought and as-built LB-PBF SS316L material was also included in the investigation, both of which were manufactured with the same composition.

2.2. Post processing Procedures

Post manufacture, all of the cylindrical/octagonal blanks were subjected to a HT procedure in order to consolidate the material and promote microstructural changes through recrystallisation prior to being

Table 1
Composition of stainless steel 316 L powder.

Element	C	Cr	Ni	Mo	Si	Fe	Mn	S	P	N	O (ppm)
(%)	0.01	16.87	12.41	2.32	0.57	base	1.2	0.002	0.008	0.11	341

Table 2
Particle size distribution of stainless steel 316 L powder.

D_x Number	Particle Size Diameter (μm)
D_1	10–16
D_{25}	20–26
D_{50}	26–32
D_{75}	34–40
D_{90}	43–49

removed from the baseplate using wire EDM. The specific parameters for the heat treatments are provided within Table 3.

Once the LB-PBF cylindrical and octagonal blanks had been heat treated, they were machined in compliance with the specimen drawings shown in Fig. 2, for LCF, FCG and tensile testing, respectively. All samples were longitudinally polished in accordance with ASTM E606 to impart a maximum of 0.2 μm surface roughness.

2.3. Microstructural characterisation

Post HT, some sample blanks were prepared using standard metallographic techniques to investigate the microstructural changes induced through HT. The process started with initial grinding and used successively finer grit cloths, concluding with an MD-Chem polishing cloth with a 0.04 μm OP-S suspension, to achieve a reflective, mirror-like finish.

The microstructures were analysed using a Hitachi SU-3500 scanning electron microscope (SEM). The texture and grain orientation were measured using electron-backscattered diffraction (EBSD). The main operating parameters selected for both techniques were 20 kV accelerating voltage and a spot size of 90. The EBSD required a step size and exposure time of 0.59 μm and 10 μs, respectively. In the interpretation of the EBSD maps, low angle boundaries (LAB) were defined as having a local misorientation $< 15^\circ$ and high angle boundaries (HAB) defined as $> 15^\circ$ misorientation. Texture analysis followed a threshold value whereby samples exhibiting maximum multiples of uniform density (MUD) values > 3, the material could therefore be regarded as containing 'crystallographic texture'. Grain size and aspect ratio measurements for all microstructures were determined using the mean linear intercept (MLI) method.

Grain orientation spread (GOS) is a key parameter for evaluating the degree of plastic deformation within individual grains and is widely used as an indicator of recrystallisation during post-processing. GOS measures the average angular misorientation between neighbouring points within a grain, as determined by the in-built algorithm in Channel5 software. Low GOS values typically correspond to fully recrystallised grains, while higher values suggest deformation or partial recrystallisation. In this study, GOS was used to quantify the extent of recrystallisation in LB-PBF SS316L samples. EBSD maps were acquired for each sample, and the grain-level misorientations were analysed to compute GOS values. Grains exhibiting GOS values below a defined threshold, commonly set at 2°, were classified as recrystallised, in line with previous studies [19]–[20] that established a strong correlation between low GOS values and complete recrystallisation. The recrystallised fraction was then determined by summing the areas of all grains with GOS values below this threshold.

2.4. Mechanical testing

2.4.1. Uniaxial tensile

Uniaxial tensile testing was conducted at Swansea Materials Research & Testing Ltd (SMaRT), an ISO 17025-accredited laboratory. Testing was carried out in accordance with BS EN ISO 6892–1 [21] and were performed at ambient room temperature using a test rate of 0.002 – 0.1 /s. The initial low strain rate enabled the use of an extensometer on the gauge section to accurately capture yield stress and Young's modulus. Beyond this point, the extensometer was removed, the strain rate was increased to 0.1/s and the test was performed at this rate until failure. Both vertical and horizontal build orientations of the LB-PBF heat-treated material and wrought SS316L were tested, with one repeat specimen included per condition.

2.4.1.1. Low cycle fatigue. Low-cycle fatigue (LCF) testing was used to

Table 3
Post manufacture heat-treatment parameters for LB-PBF SS316L geometries.

Heat Treatment	Temperature (°C)	Hold Time (Minutes)	Heating / Cooling Rate (°C/Min)
HT1	1050	135	<10
HT2	1150	135	<10
HT3	1200	135	<10

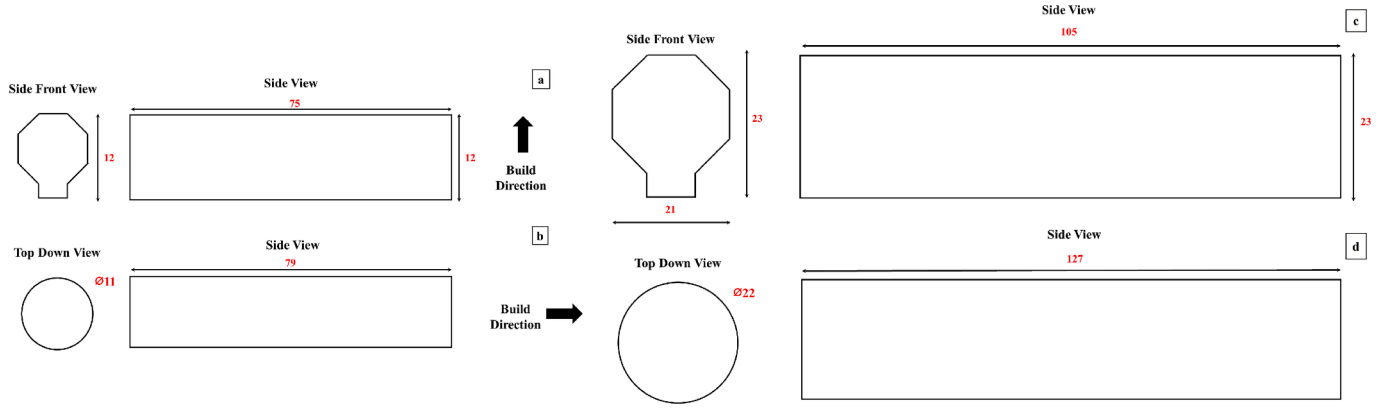

Fig. 1. Blank vertical (cylindrical) and horizontal (octagonal) LB-PBF SS316L samples; **a)** and **b)** crack propagation and uniaxial tensile sample blanks and **c)** and **d)** low cycle fatigue.

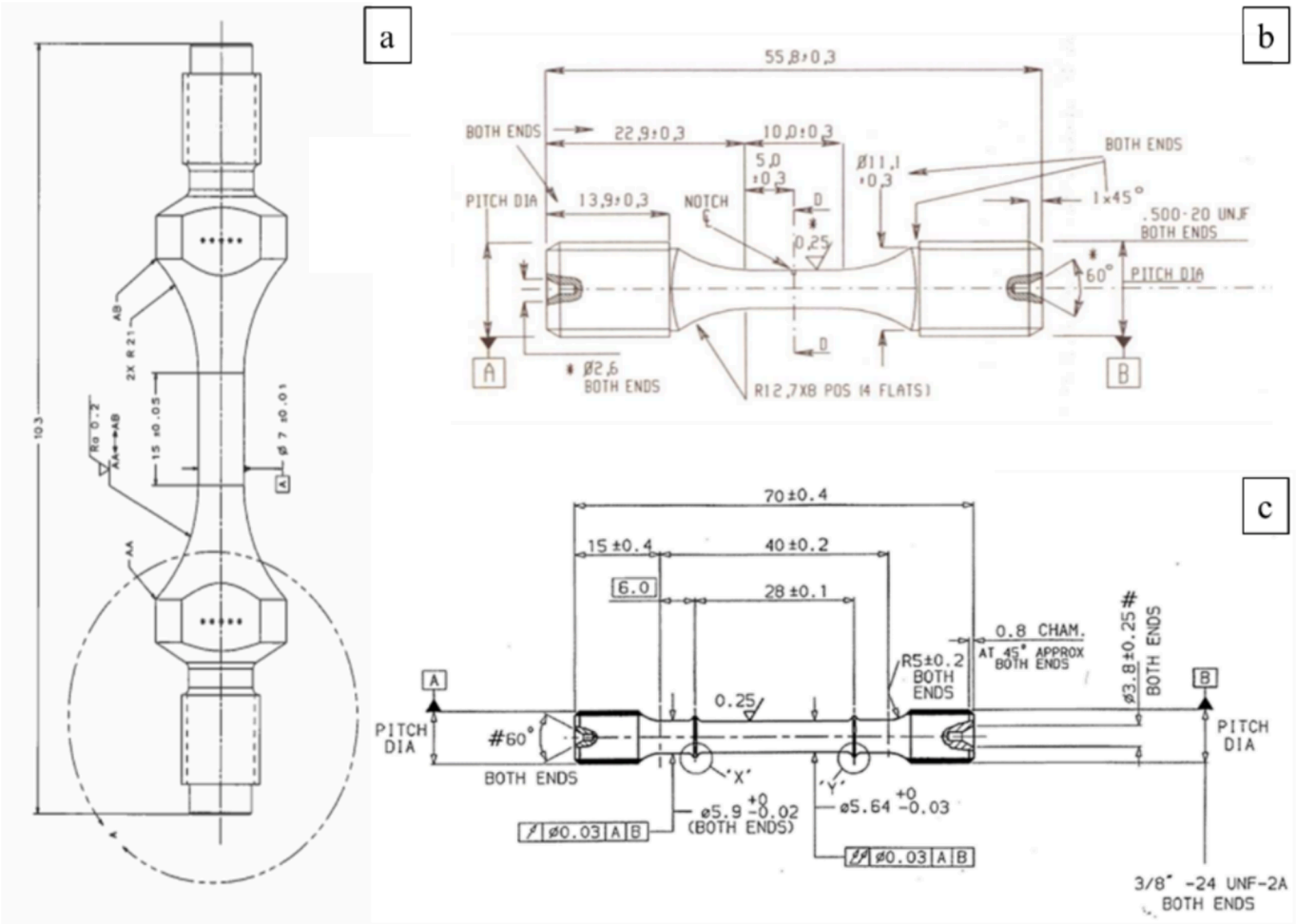

Fig. 2. Dimensional specimen drawings for **a)** low cycle fatigue, **b)** fatigue crack propagation and **c)** uniaxial tensile testing.

assess cyclic plasticity and total fatigue life as a function of heat-treatment-induced microstructural changes. All LCF tests were conducted in accordance with BS 7270 [22] within the SMaRT facility on an Instron 1341 servo-hydraulic test frame under strain-controlled conditions. Tests were performed under a triangular waveform at a strain rate of 0.4 %/s and a fully reversed loading ratio (R = − 1). Two strain amplitudes (e_a) were investigated: 0.3 % and 0.6 %. Throughout the LCF experiments, fatigue life (N_f) was defined as the number of cycles corresponding to a 25 % drop in peak load. Tests were either continued until failure or terminated at 100,000 cycles, at which point specimens were considered run-outs.

2.4.1.2. Fatigue crack growth. Fatigue crack growth (FCG) testing was conducted to independently quantify Paris-regime propagation behaviour under load-controlled conditions. The combined approach with LCF experiments enables separation of initiation-dominated and propagation-dominated effects of recrystallisation on fatigue performance.

Fatigue crack growth experiments were conducted using the direct current potential drop (DCPD) technique to monitor crack progression in real time. A constant direct current (DC) was applied across each specimen, while voltage probes were positioned adjacent to the anticipated crack path to detect changes in electrical potential. Variations in potential were continuously recorded throughout the test, enabling accurate, real-time tracking of crack extension.

All crack propagation tests adhered to ASTM E647 standards and were carried out at the SMaRT facility using an Instron 1341 servo-hydraulic testing machine. Initial pre-cracking was performed at room temperature under a stress specific to each sample, using a sinusoidal waveform at a frequency of 1 Hz and an R-ratio of − 1, until a potential drop (PD) of 10 μV was reached. Once a predefined crack length was achieved, the main propagation phase commenced, also at room temperature. During this phase, loading was applied at a reduced frequency of 0.333 Hz using a triangular waveform, again with an R-ratio of − 1, to more accurately simulate the loading conditions observed in low cycle fatigue (LCF) tests. Crack growth continued until a final PD of 450 μV was reached. Calibration was performed in advance using a dummy specimen to establish a reliable correlation between PD measurements and actual crack length.

The primary objective of the crack propagation tests was to determine the relationship between the crack growth rate (da/dN) and the stress intensity factor range (ΔK) within Stage II crack propagation. This relationship typically consists of three distinct regions: a near-threshold regime at low ΔK values where crack growth is minimal or ceases; a rapid growth regime at high ΔK values leading to final failure; and the intermediate Paris regime, where the crack growth rate follows a stable, linear trend on a log–log scale, described by the Paris law taken from [23], where C and m are constants depending on the material, temperature and stress ratio:

$$\frac{da}{dN} = C\Delta K^m \tag{2}$$

In all FCG tests, intervals of 10,000 cycles were used as a screening step to determine whether propagation was detectable by DCPD at the initial stress level; if not, the stress was increased to efficiently reach a prop-

agating condition for subsequent Paris-regime characterisation, in accordance with ASTM E647. This procedure was not intended to establish a VHCF runout threshold."

2.4.1.3. Cyclic polarisation. Cyclic polarisation tests were conducted using a Gamry 1010E potentiostat to evaluate the corrosion behaviour of LB-PBF SS316L samples subjected to the different HTs. This technique involves applying an anodic potential to the sample to induce localised corrosion and then reversing the scan once a set current is measured to observe re-passivation. From the resulting data, the passive current, the pitting potential, the point at which the passive oxide layer breaks down, and the re-passivation potential, the point at which the oxide layer re-forms, can be determined. Additionally, the free corrosion potential, (E_{corr}), representing the unperturbed electrochemical potential of the sample in the test environment, was recorded. The test medium was a 3.5 wt% NaCl (salt) solution. Samples were mounted in a circular holder, exposing a surface area of 0.36 cm^2, and served as the working electrode in a standard three-electrode setup. A saturated calomel electrode (SCE) was used as the reference electrode, and a platinum-plated electrode served as the counter electrode. The reference electrode was placed close to the working electrode to ensure accurate potential measurement. Cyclic polarisation scans began 0.2 V below E_{corr}, with a forward scan rate of 0.166 mV/s. The scan continued until a current density of 3.6 mA/cm^2 was reached, at which point the direction of the scan was reversed. The test was terminated when the voltage returned to the initial starting potential.

3. RESULTS

3.1. Microstructural behaviour

3.1.1. As-built LB-PBF & wrought SS316L

Examination of the as-built LB-PBF SS316L microstructure (Fig. 3) reveals a typical morphology commonly observed in AM materials [24]–[25]. The IPF colour maps show that the microstructure exhibits distinct characteristics depending on the plane of observation. The XY and XZ planes relative to the baseplate were cut from samples that were built vertically and horizontally.

In both the vertical and horizontally built materials, the XZ microstructural plane (parallel to the build direction) is dominated by epitaxial grain growth aligned to the build direction, resulting in elongated columnar grains that extend across multiple melt pools. This anisotropic grain structure arises from the directional solidification inherent to the LB-PBF process [26]. In contrast, the XY plane (perpendicular to the build direction) for both orientations reveals a much finer and more equiaxed grain morphology, as previously seen in other studies [27,28]. These planar differences lead to significant variation in grain size and aspect ratio across the sample. As shown in Table 4, the average grain size in the XY plane is approximately 140 μm^2, markedly smaller than the 300–400 μm^2 observed in the XZ plane. Despite differences in grain size, the two build orientations exhibit broadly similar microstructural features, with comparable values for aspect ratio and grain boundary (GB) fractions. As such, comparing the

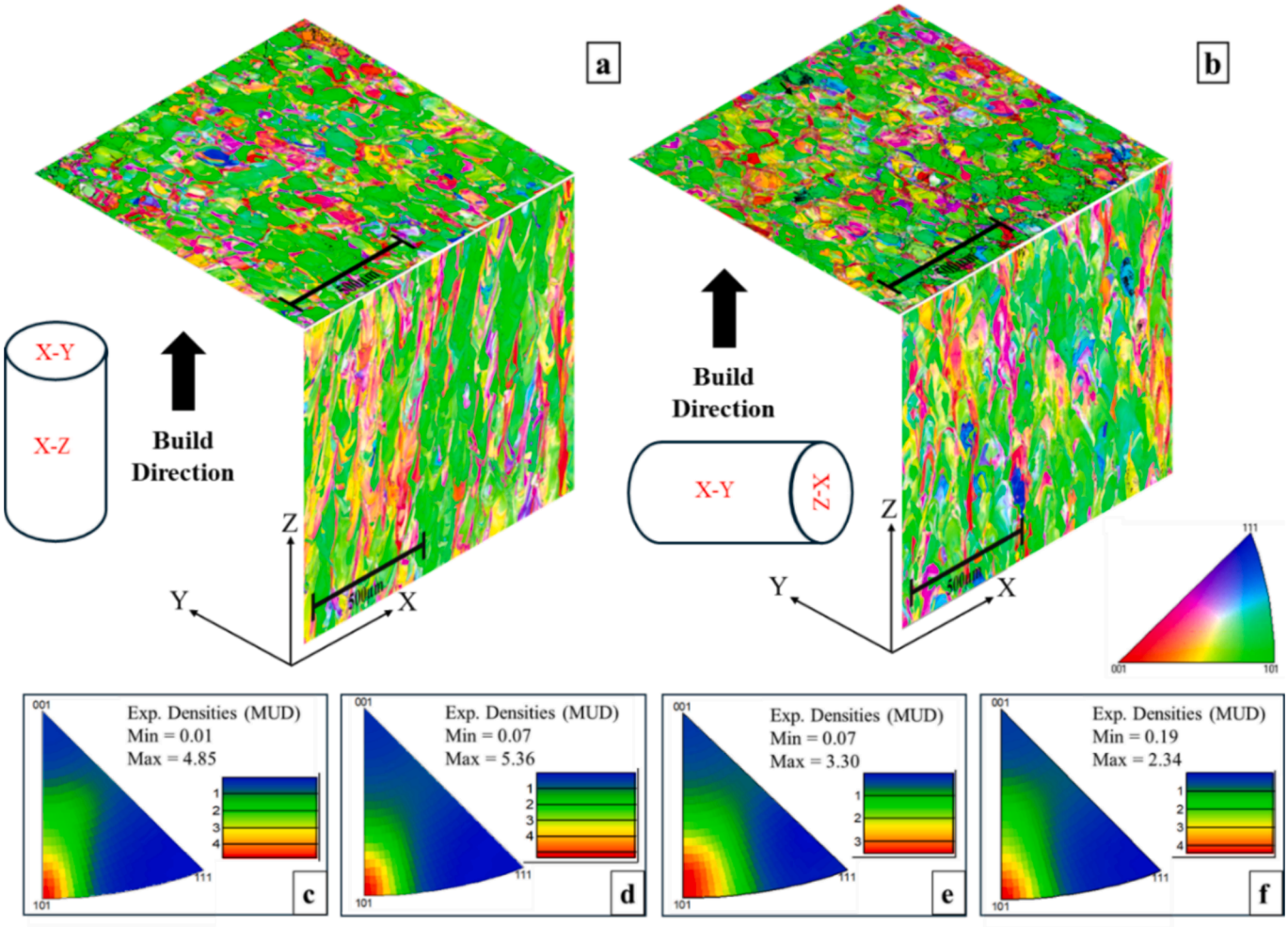

Fig. 3. EBSD IPF maps of the as-built SS316L build orientations; **a)** vertical and **b)** horizontal. Inverse pole figures of as-built SS316L; **c)** vertical XZ, **d)** vertical XY, **e)** horizontal XZ and **f)** horizontal XY.

Table 4
As-built and wrought SS316L EBSD microstructural data.

Sample		Grain size (μm²)	Aspect Ratio	LAB (%)	Σ3 (%)	Max MUD
Vertical	XZ	302	0.23	77.1	0.29	4.85
	XY	145	0.41	78.0	0.28	5.36
Horizontal	XZ	398	0.22	69.9	0.65	3.30
	XY	141	0.42	83.9	0.23	4.43
Wrought		422	0.35	1.08	76	1.24

vertical and horizontal builds on equivalent section planes (XY and XZ relative to the baseplate) shows broadly similar grain statistics within each plane; the dominant differences arise between the XY and XZ planes due to the directional solidification inherent to LB-PBF. Therefore, for clarity, results are subsequently discussed in terms of the XY and XZ planes relative to the baseplate.

Fig. 3c)-f) presents the multiples of uniform density (MUD) analysis, confirmed by the IPF maps. The images indicate a strong < 101 > crystallographic texture, as supported by the IPF colour maps, with some isolated instances of < 001 > oriented columnar grains, which appear intermittently throughout the microstructure and are distributed across the full range of IPF colouring.

While the as-built material clearly shows evidence of anisotropy, the same morphology is not observed in wrought SS316L. The IPF colour map of wrought SS316L, shown in Fig. 4(a), reveals a uniform microstructure in the XZ plane, characterised by an equiaxed grain morphology. Given the expected similarity between the XY and XZ planes, it can be inferred that the microstructure exhibits isotropic behaviour, with no significant directionality or variation between the two planar orientations. Although broadly equiaxed, the microstructure comprises a range of grain types, namely small grains with minimal twinning, small grains without twins, and larger grains containing multiple twin boundary types. These features are consistently observed across the microstructure, with some of the larger grains potentially representing abnormally grown grains. The even distribution of these grain types is further supported in the MUD analysis in Fig. 4(b), where a significantly lower maximum MUD value of 1.24 infers an isotropic microstructural behaviour with no crystallographic texture.

3.1.1.1. Effect of heat treatment. EBSD analysis of the XZ plane for a sample built in the two orientations and then subjected to HT1 (1050 °C) reveals that minimal microstructural change occurs relative to the as-built state (Fig. 5a) and b)). The microstructure remains dominated by the characteristic columnar grains typical of the LB-PBF process, with negligible signs of recrystallisation. In the XZ plane, these elongated grains continue to traverse multiple melt pools, indicating that epitaxial grain growth persists following the HT cycle. Given this outcome, it is reasonable to infer that the XY plane, while likely exhibiting smaller, more equiaxed grains due to its orientation relative to the build direction, would similarly show limited recrystallisation.

In contrast, the HT2 parameter set at 1150 °C led to near-complete recrystallisation in both vertical and horizontal build orientations, with recrystallised fractions exceeding 96 %, as illustrated in Fig. 5c) and d). This observation is corroborated by the quantitative microstructural data presented in Table 5. Interestingly, the increase in HT temperature has resulted in an increased recrystallisation percentage and a significant rise in the presence of annealing twin (Σ3) boundaries, akin to the wrought material. The microstructure shows a uniform distribution of equiaxed grains, accompanied by the complete disappearance of the elongated columnar grains typical of the as-built and HT1 microstructural conditions. The newly formed recrystallised grains have grown sufficiently to obscure the boundaries of the original additive microstructure, indicating a thorough transformation. However, although near full recrystallisation has been obtained, the microstructure retains around 3–4 % of grains with GOS higher than 2°. Therefore, it was deemed necessary that higher temperatures would promote even further recrystallisation.

Fig. 5e) and f) shows that at 1200 °C (HT3), both build orientations have undergone full recrystallisation, with the original AM grain morphology completely removed. The microstructure is now characterised by the prominent presence of large, abnormally grown grains, alongside a uniformly dispersed population of smaller equiaxed grains situated between them. This structure arises from the competitive growth dynamics during recrystallisation, where the faster-growing abnormal grains consume most of the available stored energy. Interestingly, these larger grains do not necessarily exhibit lower aspect ratios, as indicated by the values in Table 5, which are comparable to those recorded at lower heat treatment temperatures, such as 1150 °C.

At 1200 °C (HT3), the microstructure shows much higher crystallographic texture than all other samples, exhibiting a MUD value in excess of 3 (Fig. 5e)). The IPF colour map reveals a banded crystallographic texture predominantly aligned along the < 101 > direction. This suggests partial retention or reorientation of the original build texture following HT. Although the HT did promote significant recrystallisation and grain refinement, it did not fully randomise the orientation distribution. Instead, preferential grain growth likely followed the thermal gradients and solidification fronts from the as-built condition. The full microstructural data for the HT variants is displayed in Table 5.

3.2. Mechanical testing

3.2.0.1. Uniaxial tensile

Fig. 6 shows the indicative uniaxial tensile results, with a single specimen per variant plotted for each test condition at room temperature. The resulting stress–strain curves for the SS316L variants exhibited typically ductile behaviour, with the wrought material exhibiting a

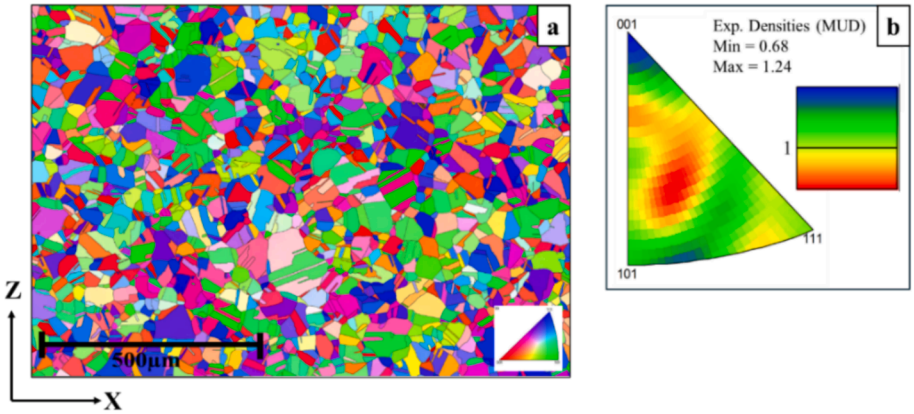

Fig. 4. Wrought SS316L **a)** EBSD IPF colour map and **b)** inverse pole figure.

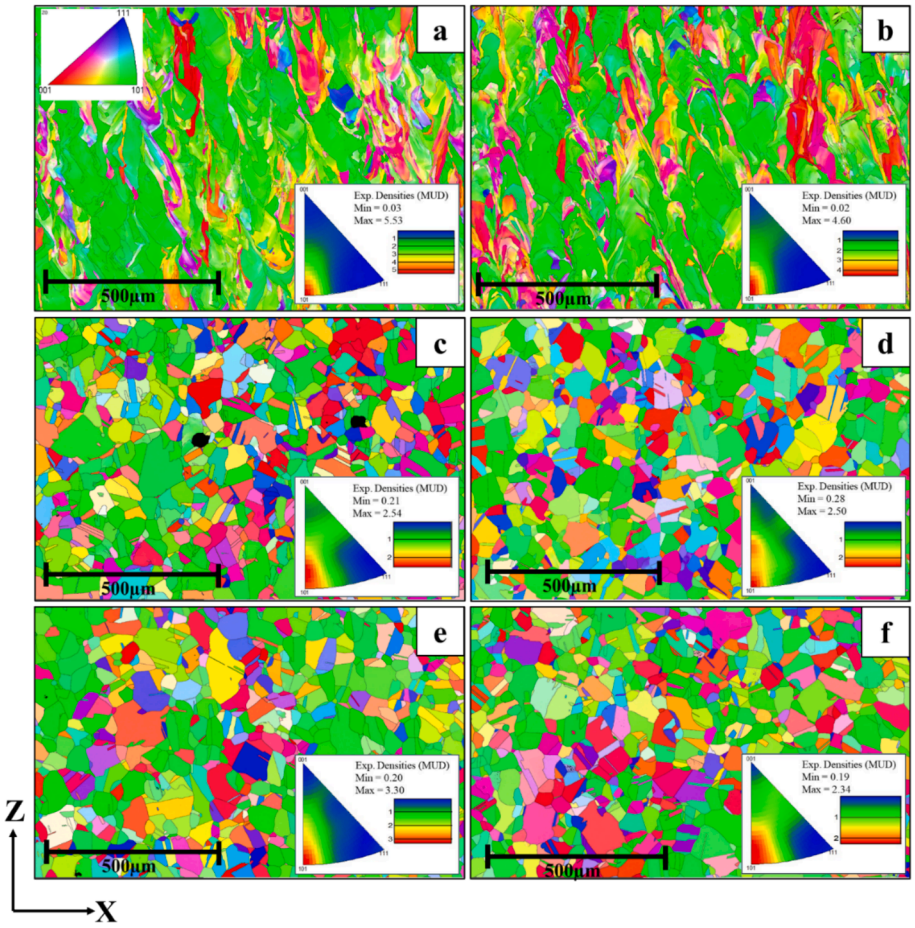

Fig. 5. EBSD IPF colour maps and inverse pole figures of XZ plane of heat treated LB-PBF SS316L. HT1 – 1050 °C **a)** vertical and **b)** horizontal build orientations. HT2 – 1150 °C **c)** vertical and **d)** horizontal build orientations. HT3 – 1200 °C **e)** vertical and **f)** horizontal build orientations.

Table 5
Heat treated LB-PBF SS316L EBSD microstructural data (all measured from the XZ plane).

HT ID	Build Orientation	Grain size (µm²)	Aspect Ratio	LAB (%)	Σ3 (%)	Rx (%)	Max MUD
HT1	Vertical	275	0.27	0.78	0.37	18.8	5.53
	Horizontal	285	0.26	0.79	0.38	17.03	4.60
HT2	Vertical	797	0.37	13.2	41.0	96.4	2.54
	Horizontal	778	0.40	11.4	70.9	98.1	2.50
HT3	Vertical	1,068	0.36	12.8	39.4	99.2	3.32
	Horizontal	902	0.35	31.7	31.3	99.9	2.30

proof stress (σ_{PS}) of 247 MPa, followed by strain hardening, and an ultimate tensile strength (σ_{UTS}) of 597 MPa. Necking occurs post-σ_{UTS}, with a final strain to failure (*SaF*) of 0.81, consistent with literature values [29,30].

The tensile behaviour of the HT1 samples (1050 °C, 135 min) highlights the orientation dependency on the mechanical properties. Horizontally built samples achieved higher σ_{UTS} (~640 MPa) and σ_{PS} (~380 MPa) values than vertically built samples (556 MPa and 361 MPa, respectively). However, vertical samples demonstrated superior ductility, with a *SaF* of 0.76, compared to 0.50 for horizontal specimens. Post σ_{UTS}, the horizontal sample showed a sharper drop in stress, indicating limited strain hardening and more abrupt failure, while vertical samples displayed a more gradual decline, suggesting enhanced plasticity. These differences reflect the anisotropic grain structures exhibited in Fig. 5, where vertical builds exhibited elongated grains along the loading direction, promoting ductility, while horizontal builds contained grains transverse to loading, resulting in reduced elongation and a more brittle mode of failure.

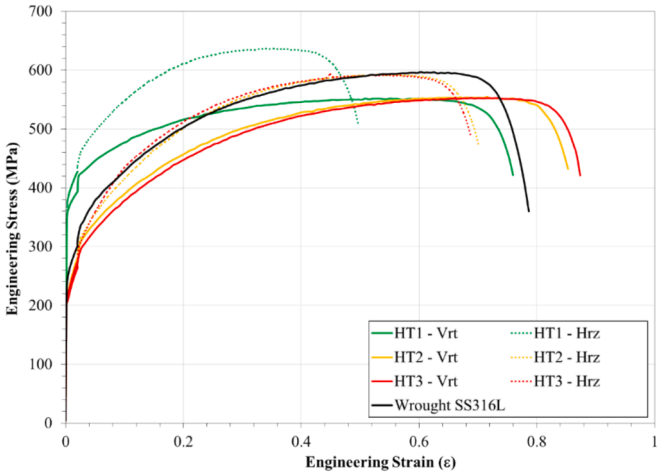

Fig. 6. Stress–strain plots for wrought and LB-PBF SS316L HT variants.

The uniaxial tensile response of near fully recrystallised LB-PBF SS316L (HT2 and HT3) in both vertical and horizontal build orientations is much different to that of HT1. These treatments exhibit significantly reduced mechanical anisotropy, indicating improved microstructural homogeneity and enhanced isotropy. Compared to HT1,

HT2 reduced the vertical–horizontal disparity by 5.6 % in σ_{PS}, 8.8 % in σ_{UTS}, and 17.7 % in *SaF*. HT3 achieved similar reductions of 3.2 %, 7.7 %, and 15.2 %, respectively. These trends reflect the increasing effectiveness of elevated-temperature homogenisation in mitigating build-orientation-dependent variability. Furthermore, irrespective of build orientation, σ_{UTS} was generally maintained to within 10 % of the HT1 condition, whilst *SaF* significantly improved, by up to 20 % in the case of the HT3 horizontal sample. This suggests that recrystallisation does not compromise the performance of vertical builds and significantly improves ductility in horizontal builds. Horizontal samples achieved a slightly higher σ_{UTS} (~590 MPa) than vertical samples (~550 MPa), but a reduced strain to failure, highlighting their inferior plastic deformation capacity. The HT3 treated samples exhibited marginally higher elongation than those treated with HT2, consistent with increased grain growth kinetics at 1200 °C.

In contrast, the σ_{PS} values see a significant drop (of more than 30 %) when comparing the HT1 results to samples subjected to HT2 and HT3. This can be directly attributed to the change in grain size morphology, where in the HT2 and HT3 samples, grains were shown to grow 2–3 times the size of those seen in the HT1 samples, and thus exhibit a reduction in the number of grain boundaries and associated barriers to dislocation motion. For both build orientations, the σ_{PS} values for HT2 and HT3 samples ranged from 207-217 MPa, with vertical specimens showing a smoother yield transition, indicative of distinct plastic behaviour. This mechanism is likely influenced by the recrystallised grain texture. Vertical samples contained banded grains aligned parallel to the loading axis, enhancing ductility, whereas in horizontal samples the grain alignment was perpendicular, contributing to higher strength but reduced elongation. The full tensile properties are also displayed in Table 6.

3.2.0.2. Low cycle fatigue

Fatigue performance was evaluated across two applied strain amplitudes, e_a = 0.3 % and 0.6 %. Fig. 7 presents the strain amplitude-fatigue life and stabilised stress range-fatigue life behaviours, revealing a significant variation in fatigue performance between vertical and horizontal build orientations, particularly under the HT1 condition. At both strain amplitudes, vertically built samples exhibited a superior fatigue performance compared to their horizontally built counterparts across all heat treatments. This disparity was most pronounced under HT1, but gradually diminished with HT2 and HT3, indicating that recrystallisation and increasing HT temperature promote microstructural homogenisation. Based on the data generated, the results indicate that generally the fatigue life of both orientations have mildly improved with HT2 and HT3, as shown by a slight rightward shift of the majority of data points across both strain amplitudes. At a fixed e_a of 0.3 %, vertical specimens consistently exhibit superior fatigue performance compared to horizontal specimens, with fatigue lives ranging from 57,714 to 69,695 cycles for the vertical orientation and 25,979 to 50,802 cycles for the horizontal orientation, across all HT conditions. At e_a = 0.6 %, vertical samples achieve fatigue lives between 5,210 and 6,603 cycles, whereas horizontal samples range from 2,916 to 4,049 cycles.

In regards to the stabilised stress range behaviour (Fig. 7b)), across all conditions, horizontal specimens sustain higher stress ranges than vertical samples, consistently exhibiting a better fatigue performance regardless of the HT applied. This disparity is again most pronounced in the HT1 condition, which exhibits the highest stress ranges overall. These behaviours corroborate the tensile results presented in Fig. 6, where the HT1 samples achieved a far higher σ_{PS} value compared to the HT2 and HT3 materials, but to the expense of ductility.

Selecting the optimal heat treatment ultimately depends on the expected loading conditions and the mechanical performance criteria for the component in question. Different applications may prioritise factors such as fatigue endurance and yield strength, whilst in other, properties such as ductility or isotropy are considered more critical. In the current study, whilst HT2 and HT3 provide fatigue lives similar to HT1, they tend to have reduced yield strength, potentially leading to earlier onset of plastic deformation. However, these treatments also allow for greater plastic strain accommodation prior to failure and improve microstructural consistency between build orientations.

Fig. 8a) and b) presents monotonic and stabilised hysteresis stress–strain responses of HT1 vertical and horizontal samples at e_a = 0.6 %, highlighting the mechanical differences between the two build orientations. Both the monotonic and stabilised loops show that the horizontal samples reach higher maximum stresses than the vertical material, which appears to yield under a lower stress in the monotonic condition. As the samples reach the stabilised condition, the horizontal sample is again achieving a greater stress range, however, the vertical sample is accruing a greater volume of plasticity, as evidenced by the greater width in the stress–strain loop. This is due to the vertical material's superior ductile properties, as seen previously in the tensile results presented in Fig. 6.

For HT2 samples (Fig. 8c) and d)), the monotonic loops show good agreement between orientations, reflecting enhanced microstructural uniformity. Yet, as the samples reach the stabilised condition, the loops start to deviate once again, with the horizontal specimen exhibiting a greater stress range (641 MPa compared to 584 MPa), reaffirming a stronger cyclic hardening response in the horizontal build direction. This indicates that some residual anisotropy still persists in the material subjected to this heat treatment, despite the microstructure appearing to be nearly fully recrystallised.

In the HT3 samples, the loop behaviours are highly comparable to those seen in the HT2 materials, as shown in Fig. 8e) and f). Some subtle differences can be seen, notably where the vertical sample exhibits a slightly wider loop in both monotonic and stabilised conditions, reaching a noticeably lower peak stress and thus indicating greater plastic deformation during the initial loading cycle. This suggests that even after full recrystallisation at 1200 °C, the build orientation continues to influence deformation behaviour, likely due to the residual microstructural features and the retained < 101 > banded texture previously identified. Therefore, whereas recrystallisation clearly reduces anisotropy, the mechanical differences between build orientations are still not fully eliminated.

These differences between the build orientations becomes more pronounced in the stabilised condition (Fig. 8f)), as the vertical sample continues to exhibit a slightly wider loop, consistent with higher plastic strain accumulation and indicative of retained anisotropy. The horizontal specimen, however, achieves a higher peak stress of 270 MPa, suggesting that cyclic hardening is still more dominant in this

Table 6
Uniaxial tensile data of all SS316L test conditions.

HT ID	HT Time (Minutes)	HT Temperature (°C)	Avg. σ_{PS} (MPa)		Avg. σ_{UTS} (MPa)		Avg. *SaF* (%)	
			Vrt	Hrz	Vrt	Hrz	Vrt	Hrz
Wrought			247		597		80.1	
1	135	1050	361	383	556	639	75.9	49
2		1150	216	217	561	595	84.9	69.9
3		1200	207	213	553	593	87	69.4

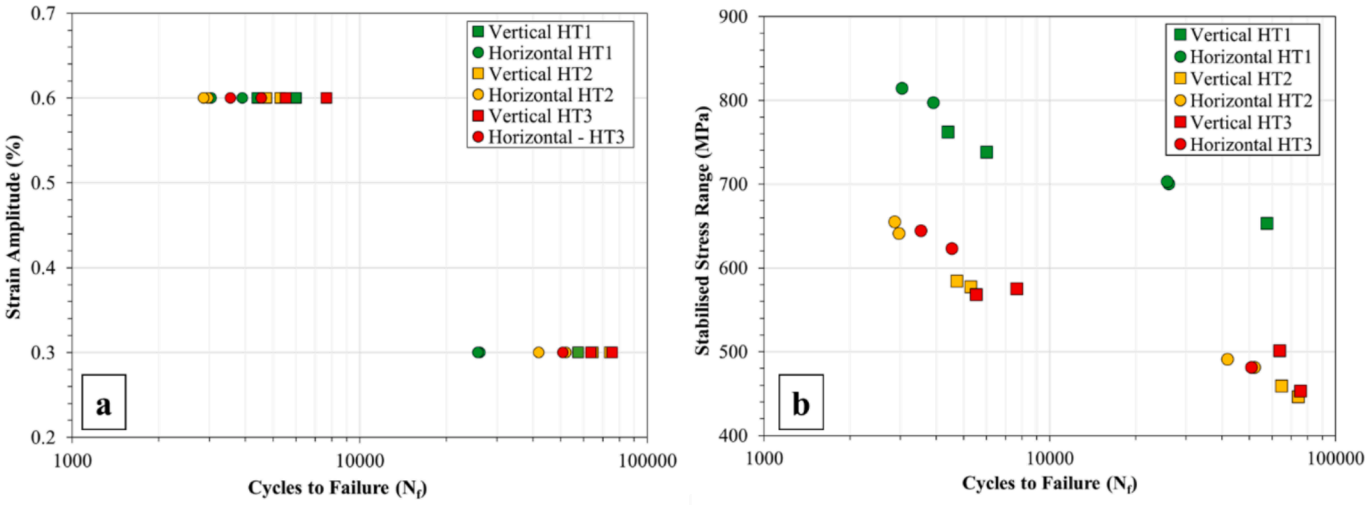

Fig. 7. LCF behaviour for LB-PBF SS316L HT variants **a)** strain amplitude and **b)** stabilised stress range.

orientation.

It should be noted however, that the hysteresis loops shown in Fig. 8 are representative examples intended to illustrate cyclic deformation behaviour, and while the observed differences between build orientations are consistent with the broader low-cycle fatigue trends (Fig. 7), they are qualitative in nature and should not be interpreted as statistically robust.

Fractographic analysis of the failed LCF samples (Fig. 9) confirms that near full recrystallisation achieved in heat treatments HT2 and HT3 has mitigated the differences in fatigue performance between vertical and horizontal LB-PBF SS316L specimens. In all tested conditions, fatigue crack initiation predominantly occurred at the surface, marking it as the primary site for stage II crack propagation. This consistent surface initiation across both recrystallised and non-recrystallised samples suggests that internal defects or sub-surface microstructural features were not the dominant factors in fatigue initiation, regardless of heat treatment condition.

For the HT1 (1050 °C) samples, the vertical sample (Fig. 9a)) reveals two distinct crack growth regions, indicating a change in fracture mode. In contrast, the horizontal sample (Fig. 9b)) shows a single, continuous crack growth region, which may relate to its reduced fatigue performance compared to the vertical build, as seen in Fig. 7. The fracture surfaces that were generated on HT2 (1150 °C) samples show two distinct crack growth regions. The horizontal sample (Fig. 9d)) appears to have a more coarse, intergranular morphology as opposed to the vertical sample (Fig. 9c)), which instead exhibited evidence of ductile shearing. For the HT3 (1200 °C) samples, the horizontal specimen (Fig. 9f)) showed an earlier onset of unstable crack growth compared to the vertical equivalent, which suggests that the vertically built material retained a superior ability to accommodate plastic deformation, thus enhancing fatigue resistance even under high strain amplitudes.

3.2.0.3. Fatigue crack growth

Across all tested material conditions, HT1 samples exhibited the greatest resistance to fatigue crack growth, maintaining the slowest propagation rates throughout the entire ΔK range. Although wrought SS316L performed better than both HT2 and HT3, it was slightly less resistant than HT1 at higher stress intensity ranges ($\Delta K > 30$ MPa·m½). This suggests that the fine, textured microstructure retained in HT1, reminiscent of the as-built condition, may offer enhanced crack deflection capabilities at elevated ΔK, despite the wrought material being more homogeneous and free of any potential manufacturing defects.

The vertical HT2 specimen showed the fastest crack growth rate, shifting into the upper portion of the *da/dN*–ΔK plot presented in Fig. 10, indicative of poor fatigue resistance. This may be attributed to its higher applied stress level of 300 MPa, increasing the stress-to-yield ratio and causing greater plastic deformation ahead of the crack tip compared to HT1, HT3, and wrought counterparts. Similarly, HT3 samples exhibited elevated crack growth rates relative to wrought material, though they remained comparable due to similar stress levels used in testing.

Both HT2 and HT3 material variants showed a more accelerated rate of crack growth with increasing ΔK, indicating reduced resistance under load-controlled cyclic conditions. Additionally, horizontally built samples from HT1 and HT3 generally displayed marginally lower crack growth rates than their vertically built counterparts, further highlighting the role of build orientation in fatigue behaviour.

It is important to note that different stress levels were required to initiate crack growth. Each test began at 250 MPa; if no crack propagation was detected after 10,000 fatigue cycles, the applied stress was increased in 50 MPa increments. Since the HT1 samples, especially those tested in the horizontal orientation, required higher stresses to initiate crack growth, they can be considered to exhibit significantly better resistance to fatigue crack propagation than the wrought material.

Fig. 11 displays EBSD maps of the crack tip regions for all tested specimens. In each case, the cracks primarily follow a transgranular path, cutting through grains rather than propagating along grain boundaries. No clear crystallographic texture guiding the crack direction is evident, suggesting that crack progression is largely controlled by localised stress fields and microstructural resistance, rather than by the alignment of specific slip systems. The cracks generally propagate perpendicular to the direction of loading, consistent with standard mode II crack propagation mechanisms.

When comparing the different microstructures, the influence of grain boundary density on crack resistance becomes apparent. As seen in Fig. 11, wrought and HT1 samples exhibit finer grains and a denser grain boundary network, as also supported from the microstructural analyses given in Figs. 4 and 5. This microstructural arrangement acts to inhibit crack growth, as boundaries help deflect the crack path, absorb energy, and blunt the crack tip. In contrast, the recrystallised HT2 and HT3 specimens exhibit coarser grains and reduced grain boundary density, offering fewer obstacles to crack progression and resulting in higher crack growth rates.

However, it is important to note that EBSD provides a two-dimensional snapshot of what is inherently a three-dimensional interaction. For HT1 specimens in particular, the visible grain boundary density likely underrepresents the actual 3D grain structure. Due to the steep thermal gradients inherent in the LB-PBF process, elongated and

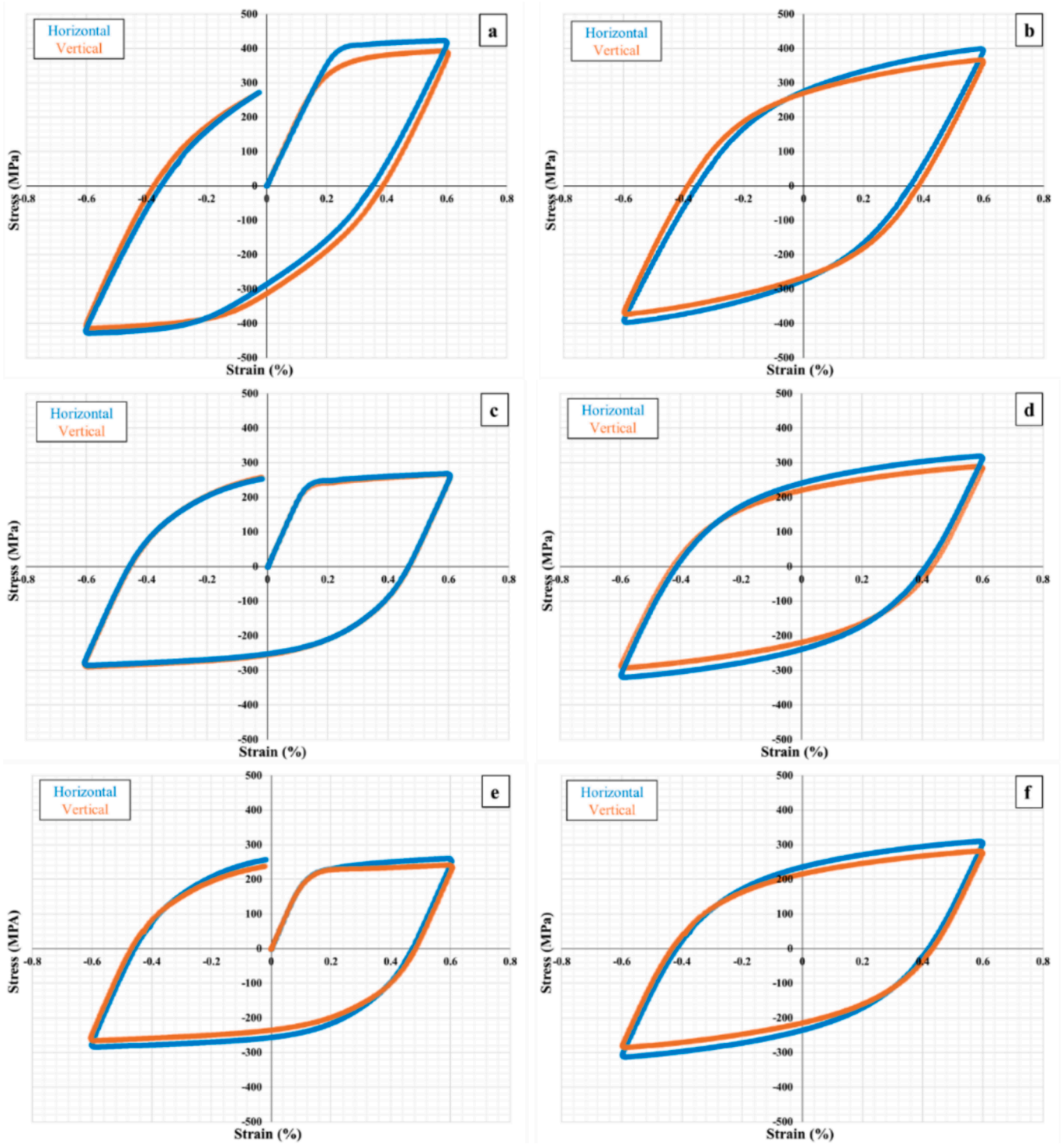

Fig. 8. LCF hysteresis stress–strain loops for LB-PBF SS316L samples tested at 20 °C, R = -1, e_a = 0.6 %. HT1 (1050 °C) **a)** monotonic, **b)** stabilised. HT2 (1150 °C) **c)** monotonic, **d)** stabilised. HT3 (1200 °C) **e)** monotonic, **f)** stabilised.

often twisted epitaxial grains form along the build direction. This complex morphology introduces additional grain boundaries in three dimensions, creating a more tortuous path for cracks, further enhancing the resistance.

3.2.0.4. Cyclic polarisation

Due to the aggressive marine environments that LB-PBF SS316L components may encounter in service, it is critical to understand how corrosion properties are influenced by heat treatment, and subsequently, whether the material is recrystallised. To evaluate this, cyclic polarisation tests were performed in a 3.5 % NaCl solution to assess the variation in corrosion performance among samples subjected to the different heat treatments.

Fig. 12 shows the cyclic polarisation curves for LB-PBF SS316L subjected to the various HTs. The recorded cyclic polarisation curves exhibited a significant change in the pitting potentials as the temperature of heat treatment was changed. The pitting potentials have been highlighted by a circle in Fig. 12 and refer to the potential at which pits

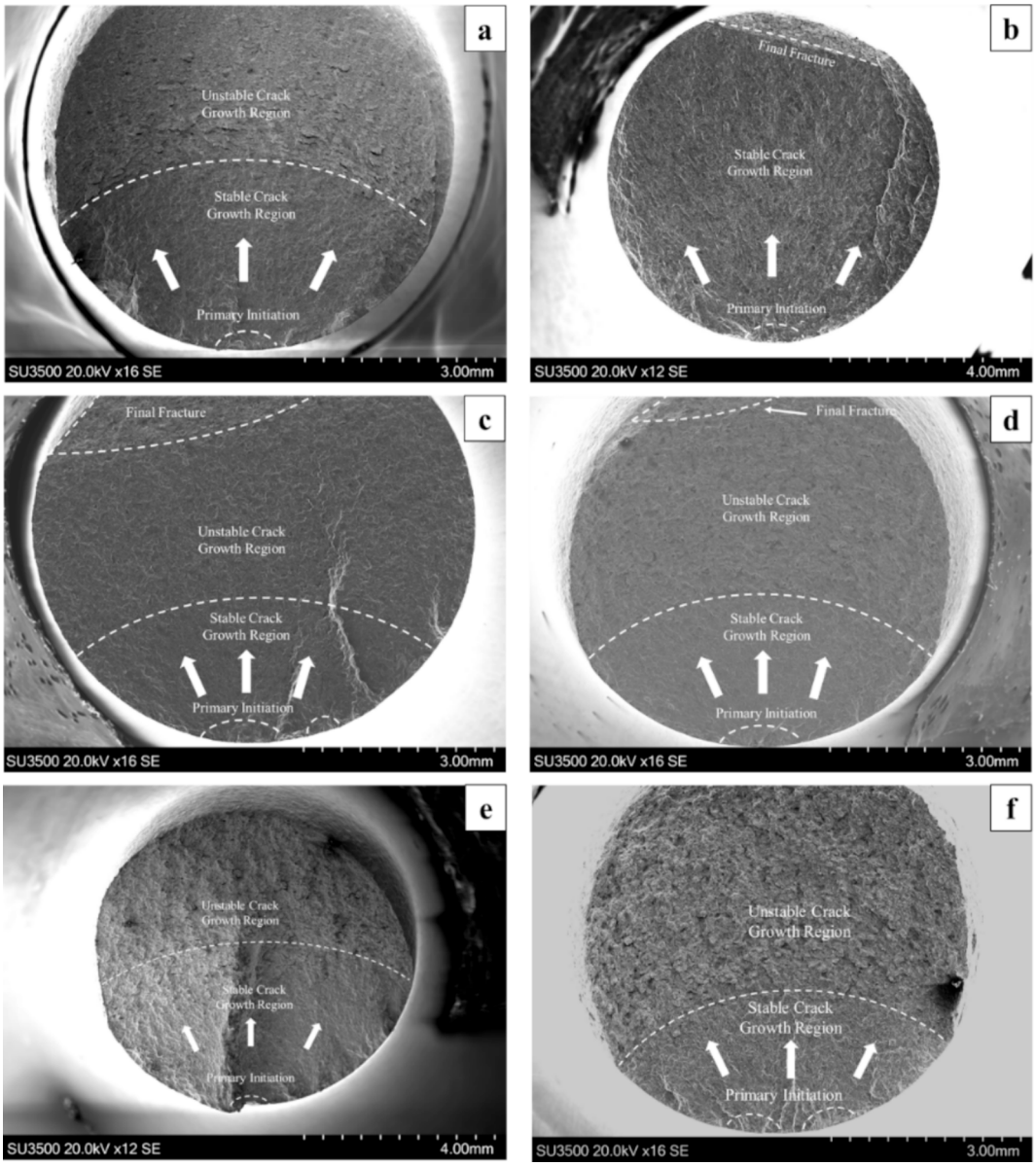

Fig. 9. Fatigue fracture surfaces of LB-PBF SS316L samples tested at 20 °C, R = -1, $e_a = 0.6$ %. HT1 – 1050 °C **a)** vertical and **b)** horizontal build orientations. HT2 – 1150 °C **c)** vertical and **d)** horizontal build orientations. HT3 – 1200 °C **e)** vertical and **f)** horizontal build orientations.

become stable and autocatalytic. HT2 and HT3 demonstrate similar E_{corr} values, approximately −0.075 V vs SCE; however, for HT1, it has been shifted towards a more negative potential, by ~ 50 mV. HT1 demonstrated a pitting potential (E_{pit}) of ~ 0.15 V vs SCE. For HT2, E_{pit} has shifted towards more positive potential by ~ 475 mV to ~ 0.625 V vs SCE, whereas for HT3, E_{pit} also has shifted towards a more positive potential by ~ 375 mV to ~ 0.525 V vs SCE.

Considering these potentials with reference to their E_{corr} values it was observed that HT2 provided the largest passive region of ~ 0.675 V compared with ~ 0.275 V for HT1 and ~ 0.625 V for HT3. Additionally, the passive current densities also changed with heat treatment, with HT3 and HT2 demonstrating the lower passive current density relative to HT1.

Based on the passive current density, the extent of the passive region and the pitting potential, it would suggest that HT2 and HT3 are advantageous regarding corrosion performance compared to HT1. However, the horizontal increasing current transients present between 0.3 V and 0.5 V vs SCE for HT3 and 0.3 V and 0.65 V for HT2 are representative of metastable pits, which initiate and re-passivate [31]. These metastable pits were much more prevalent in HT2 and HT3 compared to HT1, suggesting that the transient breakdown of the passive film may be more facile in these samples, although metastable pitting is not always an indication of the likelihood of stable pits forming.

In contrast to HT3, some *trans*-passivation was also observed after E_{pit} between 0.3 V – 0.5 V vs SCE for HT1. No re-passivation was recorded above E_{corr}, as the reverse potential was observed for all three (HT1, HT2 and HT3) experimental samples and therefore pits that have established the maximum current density of 3.6 mA/cm^2 could not re-passivate and would likely persist once established.

4. Discussion

The results chapter evaluated the impact of recrystallisation in LB-PBF SS316L samples subjected to tensile, fatigue and corrosion experiments resistance, with the aim of reducing mechanical differences between vertical and horizontal build orientations. Following on from previous work by the authors, which focussed on recrystallisation behaviour in thin walled LB-PBF SS316L structures [15], the findings

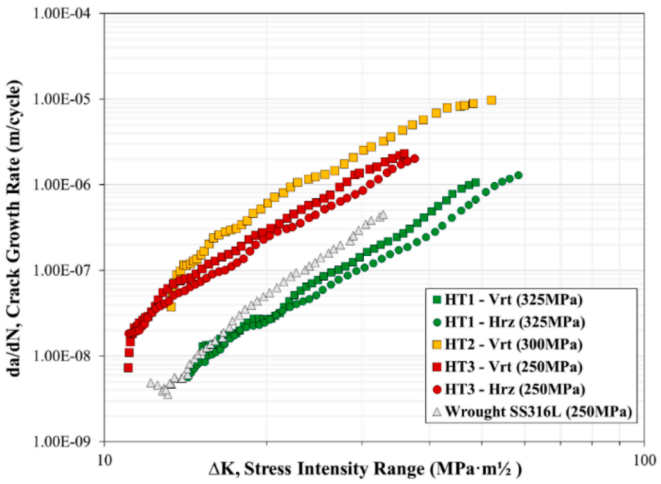

Fig. 10. Fatigue crack growth rates (*da/dN*) of the tested LB-PBF and wrought SS316L samples as a function of Δ*K* (stress intensity range).

here confirmed 1150 °C and 1200 °C as optimal annealing temperatures for achieving either near full recrystallisation with moderate grain growth (1150 °C), or full recrystallisation with more pronounced grain growth (1200 °C).

Despite being subjected to a HT temperature of 1050 °C (HT1), no evidence of recrystallisation was observed in the microstructure. Instead, the material retained many of the as-built features, including fine columnar-grain structures, textured morphology and inherent anisotropy typical of LB-PBF SS316L. However, at temperatures ≥ 1150 °C, a significant change in the microstructure was observed. At these temperatures, complete microstructural recrystallisation was evident at 1150 °C and further increased at 1200 °C, whilst also being accompanied by significant grain growth. Yet, at 1050 °C, there are several factors which promote the sluggish recrystallisation at this temperature, despite previous research [25–33] identifying that temperatures of 800–1200 °C can fully recrystallise LB-PBF SS316L. The main mechanism for static recrystallisation in LB-PBF SS316L is strain induced boundary migration (SIBM), as identified in previous research [34,35]. At elevated temperatures, recovery processes are expected to reduce stored deformation energy, which can influence recrystallisation behaviour. Previous studies have shown that the initial geometrically necessary dislocation (GND) density can significantly affect recrystallisation outcomes in AM metals [36]. In LB-PBF SS316L, rapid

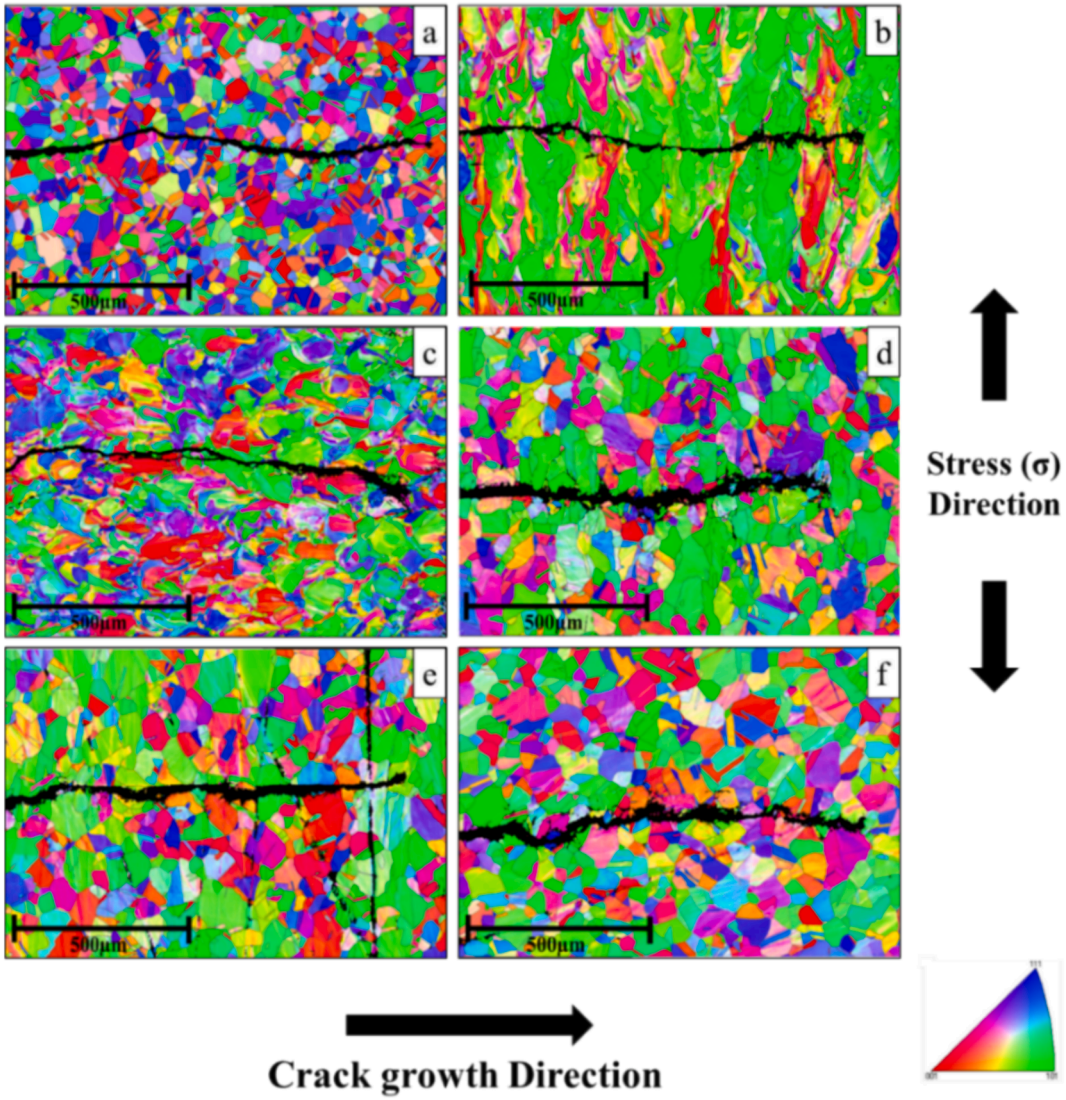

Fig. 11. EBSD IPF colourmaps of the interaction between crack tip advancement and the microstructure of tested crack propagation samples; **a)** wrought SS316L, heat treated LB-PBF SS316L **b)** HT1 vertical, **c)** HT1 horizontal, **d)** HT2 vertical, **e)** HT3 vertical and **f)** HT3 horizontal.

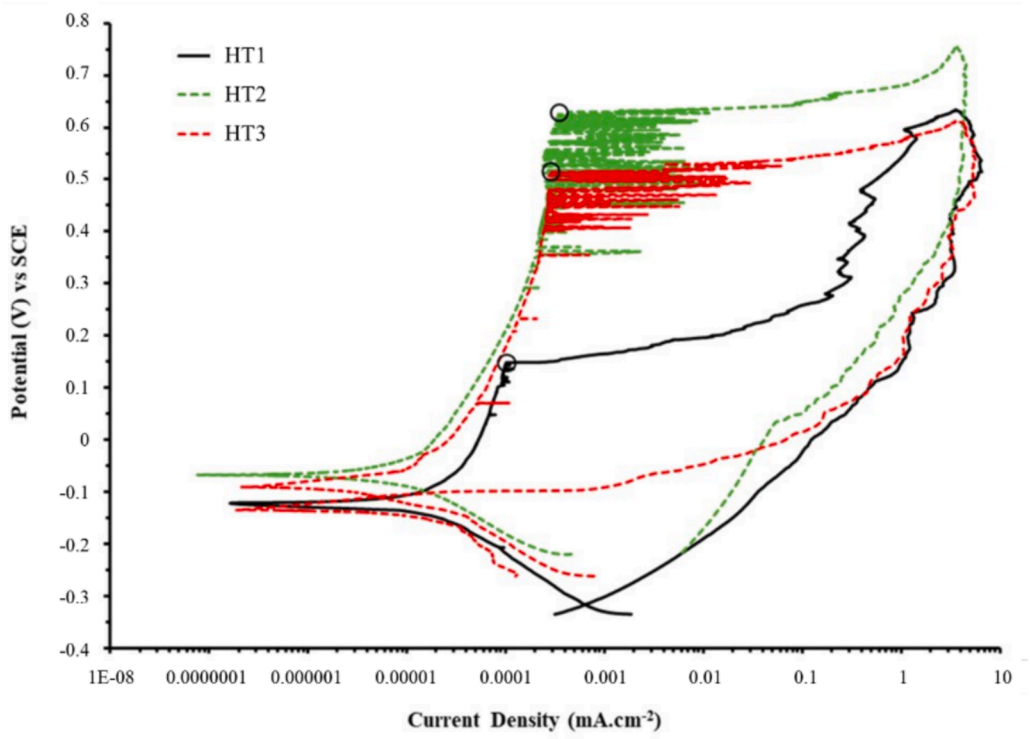

Fig. 12. Cyclic polarisation curves for LB-PBF SS316L subjected to the various HTs.

solidification and complex thermal gradients generate high dislocation densities due to residual stresses and cyclic thermal loading. Such dislocation structures are widely reported to raise stored energy, promoting recrystallisation via mechanisms such as strain-induced boundary migration (SIBM), in which low stored-energy grains invade neighbouring regions of higher stored energy [37].

However, in this study, the HT at 1050 °C did not provide sufficient thermodynamic or kinetic driving force to initiate SIBM. While this delay may partly result from variations in dislocation structures, the more plausible explanation observed in this study is the presence of oxide particles that pin grain boundaries, likely introduced through oxygen pickup during the LB-PBF process. In the as-built condition, a

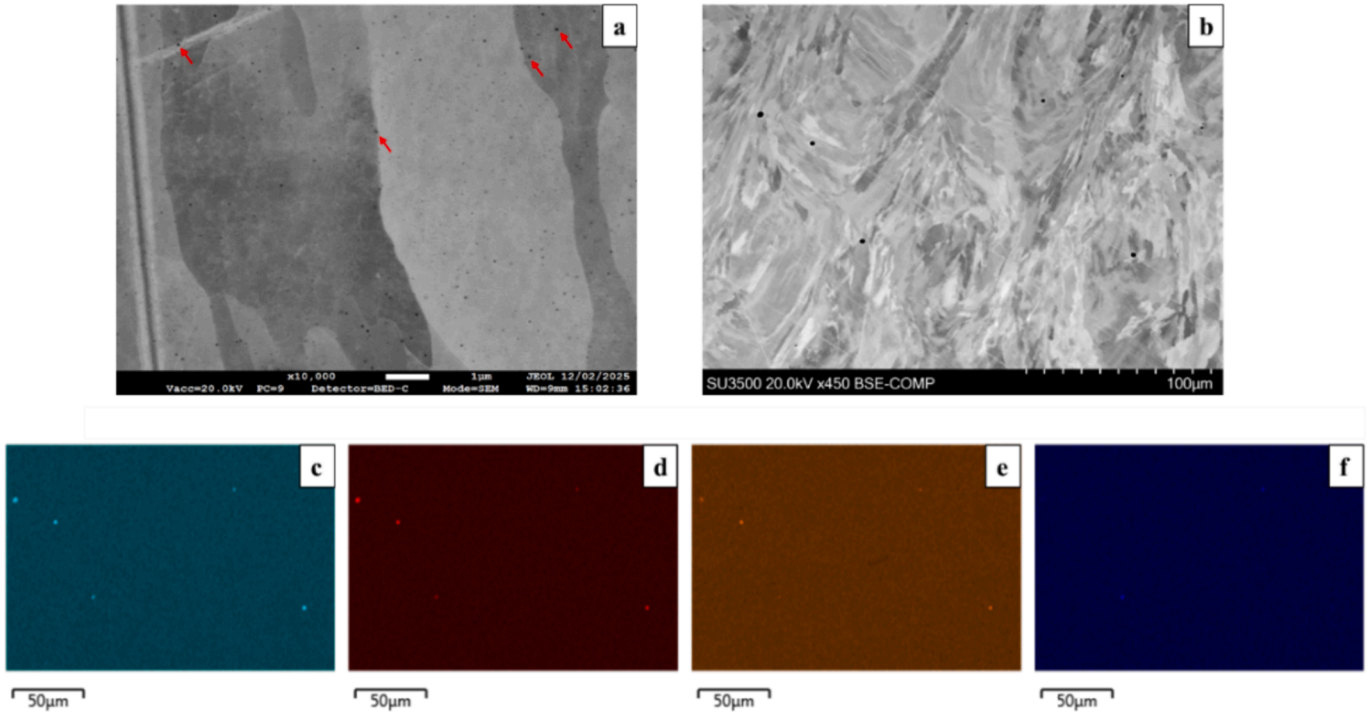

Fig. 13. As-built horizontal LB-PBF SS316L – XZ microstructural plane: **a)** high magnification of a central location, with red arrows indicating nano particles dispersed inter and transgranular, **b)** low magnification backscattered image of a central location with larger particles subjected to EDS with corresponding elemental maps **c)** O, **d)** Si, **e)** Mn and **f)** Al.

variety of relatively large oxide inclusions were identified, rich in O, Si, Mn, and Al, suggesting their formation during the build process, as shown in Fig. 13. At the current magnification, these oxides appear predominantly as larger particles. However, finer nanoscale oxides were detected under higher-resolution imaging.

During annealing, oxide particles in the microstructure are observed to coarsen, a process that is consistent with diffusion-controlled Ostwald ripening reported in the literature [38]. When a migrating grain boundary encounters these particles, its motion is temporarily arrested, while the particles themselves continue to grow via grain boundary diffusion. As particle size increases, the pinning force exerted on grain boundaries is expected to diminish, allowing previously immobilised boundaries to resume migration. This results in coarse oxide particles being left behind within recrystallised grains, often forming a visible pattern that traces the former positions of grain boundaries.

In the case of LB-PBF SS316L investigated in this study, oxides containing Si and Mn remain sufficiently fine during HT1 to effectively limit grain boundary mobility, while coarsening becomes increasingly evident at ≥1150 °C, subsequently anchoring grain boundaries and reducing their mobility, as shown in Fig. 14. During annealing, the increased atomic mobility of elements such as Si and Mn can diffuse to grain boundaries, where they react with residual oxygen to form thermodynamically stable oxides such as $MnSiO_3$ and Mn_2SiO_4. These oxides tend to nucleate at grain boundaries due to their high energy, where they exert a Zener pinning effect [39] that opposes boundary motion. Over time, diffusion-controlled coarsening mechanisms, commonly described by Ostwald ripening, promote the dissolution of smaller particles and their redeposition onto larger ones, resulting in particle growth [40]. As the oxides become larger, they lose their effectiveness at pinning, and grain boundaries that were previously immobilised are able to move once more.

This intermittent boundary movement can lead to abnormal grain growth rather than uniform recrystallisation, depending on the annealing conditions [41]. In this study, such abnormal growth was evident under the HT2 and HT3 conditions, as shown in Fig. 5. This phenomenon arises when certain grains, due to enhanced mobility or higher stored energy, grow at the expense of their neighbours, disrupting the uniformity of the grain size distribution. The presence of coarsened Si/Mn oxides contributes to this behaviour, as once grain boundaries unpin, the more mobile grains can rapidly overtake adjacent ones. Consequently, the recrystallisation process in annealed LB-PBF SS316L exhibits a staggered migration mechanism, where grain boundaries repeatedly experience cycles of pinning and unpinning influenced by Zener pinning and particle coarsening effects.

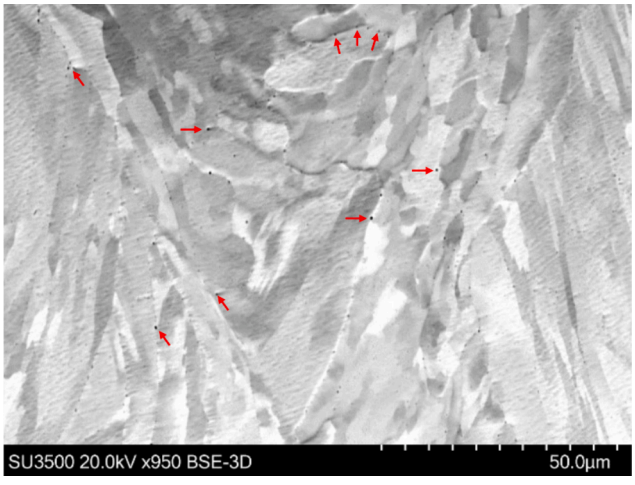

Fig. 14. Backscattered electron image showing a heavy distribution of coarsened oxide particles after HT1 conditions. Red arrows indicate presence of oxides precipitated at a variety of transgranular and intergranular locations.

Under both HT2 and HT3 conditions (Fig. 15), where near full recrystallisation has occurred, the observed patterns indicate that oxide particle coarsening via Ostwald ripening has reduced their pinning efficiency, allowing previously immobilised grain boundaries to migrate. As these boundaries advance, they may encounter and incorporate residual oxygen or other reactive species present in the microstructure or at grain boundaries. This movement promotes further oxide formation and redistribution, particularly along migrated boundaries, resulting in the increased presence of larger oxide inclusions within the recrystallised grains. This behaviour suggests that the combination of partial boundary unpinning and increased atomic diffusion during annealing facilitates both grain growth and continued oxide pickup, reinforcing the complex interplay between microstructure evolution and residual process-related chemistry in LB-PBF SS316L.

As shown in Fig. 6, tensile testing of HT1 samples revealed significant orientation-dependent differences. However, after full recrystallisation at 1150 °C (HT2) and 1200 °C (HT3), these differences were reduced by a significant amount, indicating improved microstructural consistency. Despite this, complete mechanical uniformity was not achieved, suggesting that some anisotropy remains even after high-temperature treatment.

Low-cycle fatigue testing also revealed notable differences in performance between build orientations of LB-PBF SS316L, even after HT. Vertically built specimens consistently exhibited superior fatigue life properties compared to horizontally built counterparts, likely due to residual mechanical anisotropy in the bulk microstructure. This anisotropy suggests greater resistance to cyclic loading along the build direction, where grains are aligned parallel with the applied stress. However, after full recrystallisation (HT3 at 1200 °C), fatigue performance became more consistent across both orientations. This improvement is attributed to the development of a more uniform, equiaxed grain structure at higher recrystallisation temperatures, enhancing fatigue resistance and reducing orientation dependence.

In the as-built and HT1-treated conditions, directional solidification during laser melting promotes columnar grain growth aligned along the build direction. In vertical builds, these grains align with the loading axis, implying that dislocations are enabled to travel longer distances with fewer obstacles. In contrast, horizontally built samples have grains oriented perpendicular to the load, which would shorten the mean free path for dislocations and increases resistance to deformation, potentially explaining higher yield strengths in horizontal builds.

Grain boundary strengthening also plays a key role in the mechanical performance of LB-PBF 316 L, consistent with established strengthening mechanisms in austenitic stainless steels. High-angle grain boundaries more effectively impede dislocation motion due to greater crystallographic misorientation [42], enhancing strength and fatigue resistance in recrystallised microstructures. Conversely, in insufficiently recrystallised or as-built material dominated by cellular low-angle boundaries, slip is less hindered, leading to reduced strengthening effects [43].

Fig. 16a) illustrates this effect by comparing dislocation paths in vertical and horizontal builds. In vertical samples, dislocations traverse longer paths aligned with columnar grains and face minimal boundary interference. Whereas in horizontal samples, dislocation paths intersect more grain boundaries, reducing mean free paths and increasing resistance. This grain orientation effect reinforces the observed mechanical anisotropy in HT1 samples and highlights the importance of achieving full recrystallisation to optimise fatigue performance. Fig. 16b) provides a schematic representation of the grain growth observed in fully recrystallised LB-PBF SS316L samples, comparing vertical and horizontal build orientations with respect to the loading direction. While recrystallisation is complete, the grains remain modestly elongated along their initial build axes. This subtle elongation is evident in the aspect ratios; 0.37 and 0.40 for HT2 vertical and horizontal samples, and 0.36 and 0.35 for HT3 samples as shown in Table 5. These values indicate a transition toward a more equiaxed grain morphology when compared to HT1, which suggests that recrystallisation disrupts the

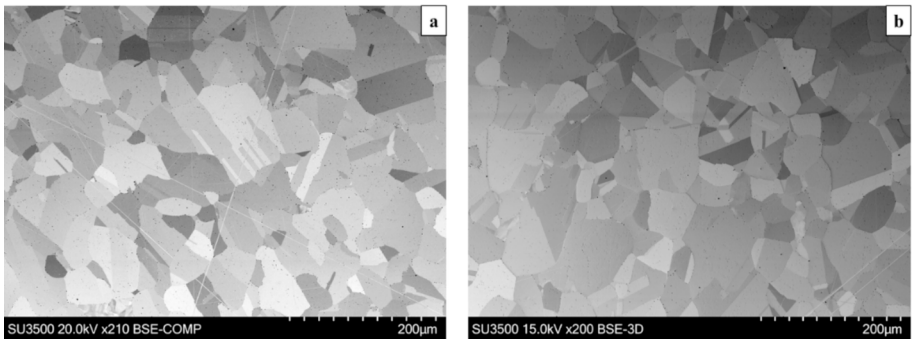

Fig. 15. Backscattered electron images showing a heavy distribution of oxide particles precipitated at transgranular and intergranular locations after heat treatment in horizontal LB-PBF SS316L samples in **a)** HT2 and **b)** HT3 conditions.

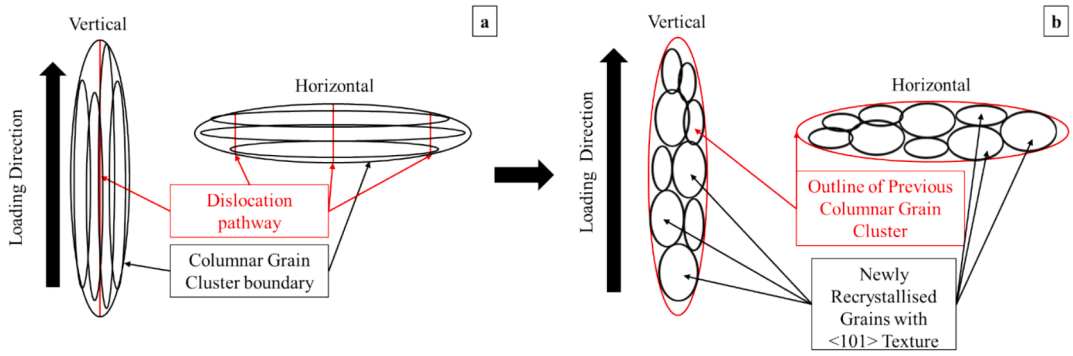

Fig. 16. Schematic images of **a)** pathway of dislocations in a columnar grained microstructure in regard to vertical and horizontal build orientation, and **b)** how newly recrystallised grains are growing in textured crystallographic 'bands', slightly aligned to build direction for vertical samples and slightly aligned perpendicular to the build direction for horizontal samples.

original columnar grain structure, promoting greater uniformity. However, mechanical anisotropy between build orientations still remains, likely due to persistent crystallographic texture or incomplete plastic strain accommodation. The slight increase in isotropy, as reflected in grain morphology, implies a more uniform deformation response, which may enhance ductility and reduce directional mechanical variation.

LCF testing further revealed that although differences in microstructural slip transfer was revealed, cracks consistently initiated from the sample surface, regardless of HT. LB-PBF SS316L is known for its high ductility, which helps redistribute stress around internal flaws, making it less susceptible to fatigue failure from subsurface defects [44]. Additionally, SS316L material built in this work was near fully density at (99.99 %), as supported by a previous body of work with comparable energy density, powder and machine parameters [45], suggesting that internal voids were too small or sparse to significantly influence fatigue life. As a result, surface flaws were the dominant sites of crack initiation in all fatigue-tested specimens. Therefore, the only limiting factor for fatigue life is the effect of the HT on the microstructure.

Fig. 11 presented representative crack-tip morphologies for LB-PBF SS316L subjected to the different heat-treatment conditions. While coarse grains are often reported to promote crack deflection and tortuosity in some materials and loading regimes, the present results indicate that this effect is not dominant in the current system. Instead, HT2 and HT3 exhibit higher fatigue crack-growth rates than HT1, consistent with the reduced grain boundary density resulting from recrystallisation and grain growth. The coarser, more equiaxed microstructures produced at higher annealing temperatures provide fewer grain boundary obstacles per unit crack advance, thereby reducing opportunities for crack deflection or arrest. In addition, the lower yield strength of HT2 and HT3 increases the size of the plastic zone ahead of the crack tip, promoting more homogeneous plastic deformation and facilitating transgranular crack propagation. HT2, in particular, exhibits the poorest crack-growth resistance, likely due to its near fully recrystallised, bimodal microstructure combined with a relatively low oxide particle density, which together offer limited resistance to crack advance. By contrast, HT3, while also coarse-grained, contains a higher concentration of oxide inclusions, particularly along grain boundaries, which may locally promote crack-path deflection or blunting, as evidenced by secondary cracking and irregular crack fronts. Although these oxides partially mitigate the detrimental effects of grain coarsening, their influence does not match the high crack-growth resistance provided by the finer, as-built-like microstructure retained in HT1, where a high density of grain boundaries and higher yield strength act to limit crack-tip plasticity and impede crack advance. Overall, these observations indicate that, in the present study, grain boundary density and crack-tip plasticity exert a stronger influence on Paris-regime crack propagation than grain-scale crack deflection effects alone.

Cyclic polarisation testing revealed that full recrystallisation of the LB-PBF SS316L microstructure resulted in higher pitting potentials, suggesting improved resistance to localised corrosion. In-situ imaging captured prior to polarisation and up to the onset of pitting initiation (Fig. 17) provided further insight into the underlying mechanisms. For HT1, pit initiation was predominantly observed along grain boundaries, which is consistent with boundary regions acting as preferential sites due to their higher energy state and the presence of fine oxides. In contrast, for HT2 and HT3 pitting was more commonly associated with intragranular regions, often appearing within grains that exhibited a cellular substructure relating to a very small percentage of retained AM grains. This shift in initiation sites can be linked to the very low proportion of un-recrystallised grains present in HT2 and HT3, which reduces the susceptibility of grain boundaries to serve as nucleation points. Instead, residual heterogeneities, such as AM grains, within the fully recrystallised grains, appear to dominate pit initiation.

High-resolution imaging (Fig. 18) revealed distinct differences in pit

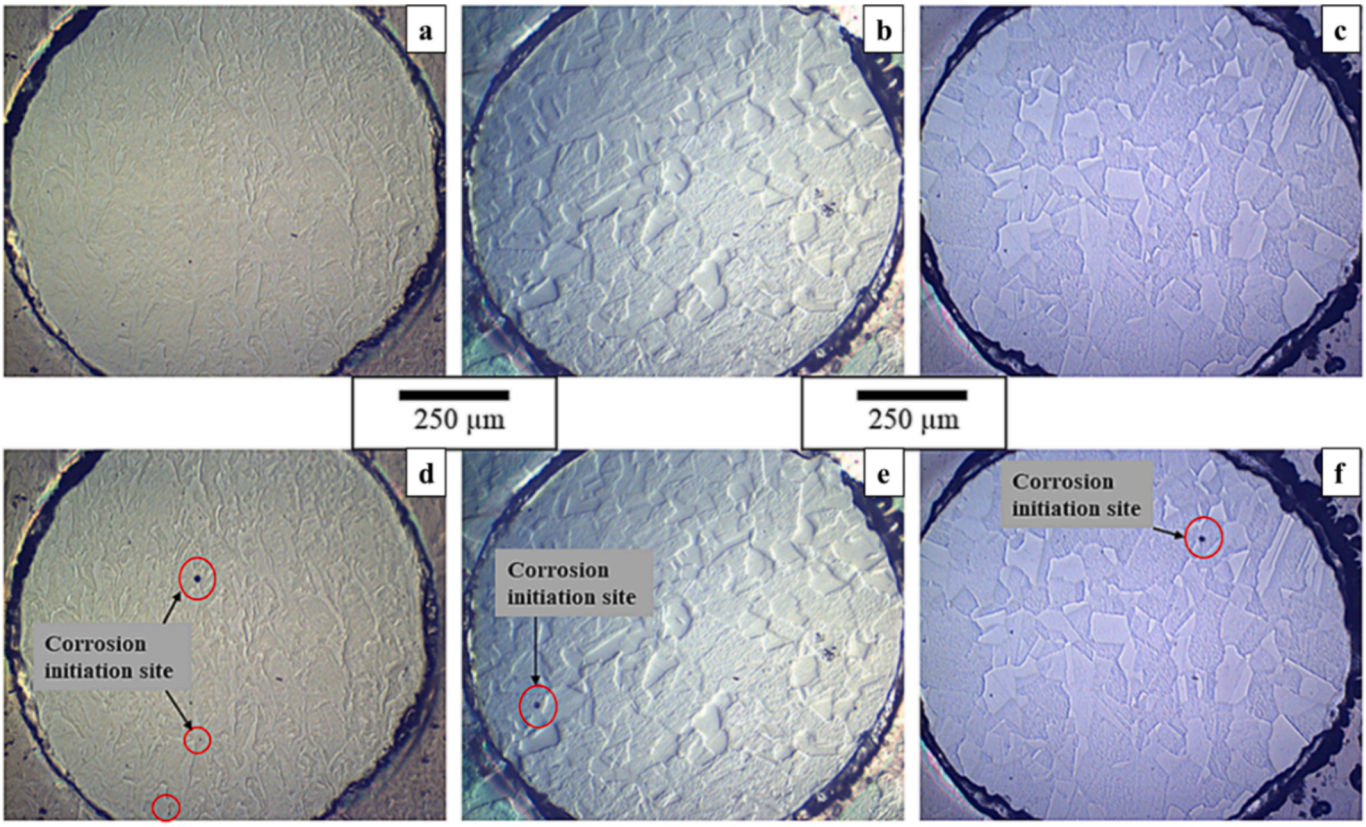

Fig. 17. Optical microscopy images taken in-situ prior to polarisation of **a)** HT1, **b)** HT2 and **c)** HT3 surfaces. Optical microscopy images taken in-situ after anodic polarisation up to the point where pitting initiated on **d)** HT1, **e)** HT2 and **f)** HT3 surface.

morphology between heat treatments. Samples subjected to HT1 exhibited more advanced pit development, frequently displaying the characteristic lacey pit morphology typical of stainless steels [46]. In contrast, pits observed in HT2 were less developed at comparable exposure times. This difference can be attributed to the finer grain size and lower levels of recrystallisation present in HT1, which result in a higher density of grain boundaries and dislocations. These features are known to act as preferential sites for passive film breakdown [47] where chloride ions can penetrate [48], while oxides disrupt film uniformity or form micro-galvanic couples [49]. The higher density of nanoscale oxide particles in HT1 may further exacerbate this effect by providing additional initiation sites for pit nucleation. Together, these heterogeneities promote metastable pit nucleation, explaining the lower E_{pit} value and more aggressive pit morphologies.

By contrast, HT2 and HT3 exhibited coarser grains, lower dislocation densities, and fewer grain boundaries, reducing preferential initiation sites. Pit initiation shifted from grain boundaries to intragranular heterogeneities such as retained cellular substructures, such as regions of non-recrystallised AM grains, or larger oxides. Although these features remain active, their lower density decreases the likelihood of widespread pit formation. Fewer, larger inclusions also pose less risk than the dense oxide population in HT1, consistent with the higher E_{pit} values in Fig. 12.

It is important to note, however, that differences in pit morphology between HT1 and HT2 may also reflect the stage of pit evolution. Given sufficient exposure time, pits in HT2 are also expected to develop into lacey morphologies. This interpretation aligns with electrochemical data, where HT1 demonstrated a lower pitting potential relative to HT2, consistent with earlier pit initiation and more aggressive propagation. Thus, while the dominant factor appears to be the extent of recrystallisation and associated defect/oxide density, pit morphology may additionally reflect the relative stage of pit development.

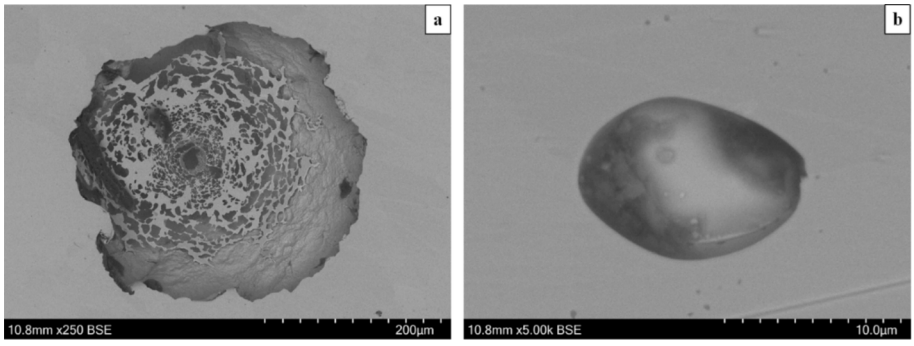

Fig. 18. Back scattered electron images of the pit formation at similar exposure times in **a)** HT1 sample showing a 'lacey-like' pit formation and **b)** HT2 showing a more hemi-spherical pit formation of much smaller magnitude.

5. Conclusions

This study investigated the effect of three post-build heat-treatment regimes on the recrystallisation behaviour and performance of LB-PBF SS316L. The key findings are as follows:

- Heat treatment at 1050 °C (HT1) produced no significant microstructural change relative to the as-built condition. Increasing the temperature above 1100 °C activated strain-induced boundary migration (SIBM), resulting in near-complete recrystallisation at 1150 °C (HT2) and full recrystallisation with pronounced grain growth at 1200 °C (HT3).
- Recrystallisation was governed by SIBM, with grain boundary motion at lower temperatures constrained by Zener pinning from fine oxide dispersions. At $\geq$ 1150 °C, oxide coarsening reduced pinning effectiveness, enabling intermittent high-angle grain boundary migration and rapid recrystallisation.
- Mechanical anisotropy was pronounced at 1050 °C, with horizontal builds exhibiting higher strength and lower ductility than vertical builds. Annealing at 1150 °C and 1200 °C reduced this anisotropy by approximately 25 %, although some directional dependence persisted, indicating that recrystallisation alone does not fully homogenise tensile behaviour.
- Low-cycle fatigue testing confirmed that anisotropy remained after annealing. While fully recrystallised microstructures did not degrade fatigue life, the 1200 °C treatment improved fatigue consistency and reliability across build orientations.
- Crack propagation resistance was greatest in the HT1 condition, attributed to the fine, as-built-like microstructure and higher yield strength, which limited plastic deformation ahead of the crack tip. This suggests HT1 is advantageous for load-controlled applications prioritising strength and crack resistance.
- Full recrystallisation improved corrosion resistance by shifting pit initiation from grain boundaries to intragranular sites and increasing pitting potential. Grain size, oxide distribution, and recrystallisation state were identified as the dominant factors controlling pitting behaviour.

Overall, the results demonstrate a trade-off between strength and crack resistance at lower temperatures and improved isotropy, fatigue reliability, and corrosion performance at higher annealing temperatures, providing a framework for tailoring post-processing routes to application-specific requirements.

CRediT authorship contribution statement

Charlie Bevan: Writing – original draft, Methodology, Investigation, Formal analysis, Data curation. **Thomas Jones:** Supervision, Project administration, Methodology, Investigation, Funding acquisition. **Amar Malla:** Investigation, Formal analysis, Data curation. **James Sullivan:** Writing – original draft, Methodology, Formal analysis, Data curation. **David Penney:** Writing – original draft, Formal analysis, Data curation. **Robert Lancaster:** Writing – original draft, Supervision, Resources, Project administration, Methodology, Funding acquisition.

Declaration of competing interest

The authors declare that they have no known competing financial interests or personal relationships that could have appeared to influence the work reported in this paper.

Acknowledgements

The current research was exclusively funded by Rolls-Royce plc. The provision of a research bursary, materials, and supporting information from Rolls-Royce plc. is gratefully acknowledged. The authors would also like to thank James Thomas and Cléophée Raoul for their assistance with the experimental setup and practical aspects of the work.

Data availability

The data that has been used is confidential.

References

[1] W. Abd-Elaziem, S. Elkatatny, A.E. Abd-Elaziem, M. Khedr, M.A. Abd El-Baky, M. A. Hassan, M. Abu-Okail, M. Mohammed, A. Järvenpää, T. Allam, A. Hamada, On the current research progress of metallic materials fabricated by laser powder bed fusion process: a review, J. Mater. Res. Technol. 20 (Sep. 2022) 681–707, https://doi.org/10.1016/J.JMRT.2022.07.085.
[2] P.A. Hooper, Melt pool temperature and cooling rates in laser powder bed fusion, Addit. Manuf. 22 (Aug. 2018) 548–559, https://doi.org/10.1016/j.addma.2018.05.032.
[3] A.J. Godfrey; Simpson, J.; Leonard, D.; Sisco, K.; Dehoff, R.R.; and Babu, S.S.; , 'Heterogeneity and Solidification Pathways in Additively Manufactured 316L Stainless Steels', *Metall. Mater. Trans. A Phys. Metall. Mater. Sci.*, vol. 53, no. 9, pp. 3321–3340, Sep. 2022, doi: 10.1007/s11661-022-06747-6.
[4] A. Fedorenko, B. Fedulov, Y. Kuzminova, S. Evlashin, O. Staroverov, M. Tretyakov, E. Lomakin, I. Akhatov, Anisotropy of mechanical properties and residual stress in additively manufactured 316l specimens, Materials 14 (23) (2021) Dec, https://doi.org/10.3390/ma14237176.
[5] F. Careri, R.H.U. Khan, C. Todd, M.M. Attallah, Additive manufacturing of heat exchangers in aerospace applications: a review, Appl. Therm. Eng. 235 (Nov. 2023) 121387, https://doi.org/10.1016/J.APPLTHERMALENG.2023.121387.
[6] F. Khodabakhshi, M.H. Farshidianfar, A.P. Gerlich, M. Nosko, V. Trembošová, A. Khajepour, Microstructure, strain-rate sensitivity, work hardening, and fracture behavior of laser additive manufactured austenitic and martensitic stainless steel structures, Mater. Sci. Eng. A 756 (May 2019) 545–561, https://doi.org/10.1016/J.MSEA.2019.04.065.
[7] R.I. Revilla, G. Li, R. Pion, K. Marcoen, F. Andreatta, L. Fedrizzi, K. Vanmeensel, I. De Graeve, Effect of heat treatment on the microstructure and pitting corrosion behavior of 316L stainless steel fabricated by different additive manufacturing methods (L-PBF versus L-DED): Comparative investigation exploring the role of microstructural features on passivity, Corros. Sci. 228 (Mar. 2024) 111814, https://doi.org/10.1016/J.CORSCI.2023.111814.
[8] M.J. Heiden, L.A. Deibler, J.M. Rodelas, J.R. Koepke, D.J. Tung, D.J. Saiz, B. H. Jared, Evolution of 316L stainless steel feedstock due to laser powder bed fusion process, Addit. Manuf. 25 (Jan. 2019) 84–103, https://doi.org/10.1016/J.ADDMA.2018.10.019.
[9] T. DebRoy, H.L. Wei, J.S. Zuback, T. Mukherjee, J.W. Elmer, J.O. Milewski, A. M. Beese, A. Wilson-Heid, A. De, W. Zhang, Additive manufacturing of metallic components – process, structure and properties, Prog. Mater Sci. 92 (Mar. 2018) 112–224, https://doi.org/10.1016/J.PMATSCI.2017.10.001.
[10] R.F. Davis, 'Hot Isostatic Pressing', *Concise Encyclopedia of Advanced Ceramic Materials*, pp. 210–215, Jan. 1991, doi: 10.1016/B978-0-08-034720-2.50061-7.
[11] A. du Plessis, P. Rossouw, Investigation of porosity changes in cast ti6al4v rods after hot isostatic pressing, J. Mater. Eng. Perform. 24 (8) (Aug. 2015) 3137–3141, https://doi.org/10.1007/s11665-015-1580-4.
[12] I.S. Grech, J.H. Sullivan, R.J. Lancaster, J. Plummer, N.P. Lavery, The optimisation of hot isostatic pressing treatments for enhanced mechanical and corrosion performance of stainless steel 316L produced by laser powder bed fusion, Addit. Manuf. 58 (Oct. 2022), https://doi.org/10.1016/j.addma.2022.103072.
[13] J.R. Davis (Ed.), *Stainless Steels*, ASM International, OH, USA, 1994.
[14] A.J. Sedriks, *Corrosion of Stainless Steels*, 2nd ed. New York, USA, 1996.
[15] C. Bevan, N. Barnard, T. Jones, R. Lancaster, Effect of heat treatment on the recrystallisation of thin-walled stainless steel 316L fabricated by laser beam powder bed fusion, Mater. Des. 258 (Oct. 2025) 114592, https://doi.org/10.1016/J.MATDES.2025.114592.
[16] W.-Y. Wang, A. Godfrey, W. Liu, Effect of heat treatment on microstructural evolution in additively manufactured 316L stainless steel, Metals (basel) 13 (6) (Jun. 2023) 1062, https://doi.org/10.3390/met13061062.
[17] C. Kirk, W. Xie, S. Das, B. Ferguson, C. Wu, H.-C. Man, C.-W. Chan, Microstructure, porosity, and bending fatigue behaviour of PBF-LB/M SS316L for Biomedical applications, Metals (basel) 15 (6) (Jun. 2025) 650, https://doi.org/10.3390/met15060650.
[18] W. Li, L. Meng, X. Niu, W. Zhou, Microstructure, mechanical properties, and deformation behaviour of LPBF 316L via post-heat treatment, Virtual Phys. Prototyp. 19 (1) (2024) Dec, https://doi.org/10.1080/17452759.2024.2405623.
[19] L. Cui, S. Jiang, J. Xu, R.L. Peng, R.T. Mousavian, J. Moverare, Revealing relationships between microstructure and hardening nature of additively manufactured 316L stainless steel, Mater. Des. 198 (Jan. 2021) 109385, https://doi.org/10.1016/J.MATDES.2020.109385.
[20] A. Ayad, N. Allain-Bonasso, N. Rouag, F. Wagner, Grain orientation spread values in if steels after plastic deformation and recrystallization', in *Materials Science Forum*, Trans Tech Publications Ltd, 2012, pp. 269–272. doi: 10.4028/www.scientific.net/MSF.702-703.269.
[21] BS EN ISO 6892-1:2019: Metallic materials. Tensile testing - Method of test at room temperature'. British Standards Institution, London, 2020.

[22] ISE/101/6. BS 7270:2006 Metallic materials. Constant amplitude strain controlled axial fatigue. Method of test. BSI, 2006.
[23] D. Liu, D.J. Pons, Crack propagation mechanisms for creep fatigue: a consolidated explanation of fundamental behaviours from initiation to failure, Metals (basel) 8 (8) (2018) Aug, https://doi.org/10.3390/met8080623.
[24] X. Tong, C. Lu, Z. Huang, C. Zhang, F. Chen, Microstructures and mechanical properties of crack-free 316L stainless steel and Inconel 625 joint by using Laser Engineered Net Shaping, Opt. Laser Technol. 155 (Nov. 2022), https://doi.org/10.1016/j.optlastec.2022.108357.
[25] S. Ren-ho, X. Jian-ying, H. Dong-po, Characteristics of Mechanical Properties and Microstructure for 316L Austenitic Stainless Steel', 2011. [Online]. Available: www.sciencedirect.com.
[26] D. Riabov, A. Leicht, J. Ahlström, E. Hryha, Investigation of the strengthening mechanism in 316L stainless steel produced with laser powder bed fusion, Mater. Sci. Eng. A 822 (Aug. 2021) 141699, https://doi.org/10.1016/J.MSEA.2021.141699.
[27] W. Li; Meng, L.; Niu, X.; and Zhou, W.; , 'Microstructure, mechanical properties, and deformation behaviour of LPBF 316L via post-heat treatment', *Virtual Phys. Prototyp.*, vol. 19, no. 1, 2024, doi: 10.1080/17452759.2024.2405623.
[28] P. Krakhmalev; Fredriksson, G.; Svensson, K.; Yadroitsev, I.; Yadroitsava, I.; Thuvander, M.; and Peng, R.; , 'Microstructure, solidification texture, and thermal stability of 316 L stainless steel manufactured by laser powder bed fusion', *Metals*, vol. 8, no. 8. MDPI AG, Aug. 15, 2018. doi: 10.3390/met8080643.
[29] Y. Wang, Q. Hou, X. Li, Z. Li, F. Wu, S. Chen, C. Lv, Q. He, X. Ye, Y. Yu, J. Hu, Strain rate-dependent tensile response and deformation mechanism of laser powder bed fusion 316L stainless steel, Mater. Sci. Eng. A 893 (Feb. 2024) 146124, https://doi.org/10.1016/J.MSEA.2024.146124.
[30] Y.K. Kim, S.H. Shim, Y.K. Kim, K. Ram Lim, Y.S. Na, Simultaneously improved strength and ductility yet strain-hardenable 316L stainless steel by sigma phase and hetero-structuring, Mater. Des. 243 (Jul. 2024) 113058, https://doi.org/10.1016/J.MATDES.2024.113058.
[31] G.S. Frankel, Pitting corrosion of metals: a review of the critical factors, J. Electrochem. Soc. 145 (6) (Jun. 1998) 2186–2198, https://doi.org/10.1149/1.1838615.
[32] F.C. Pinto; Aota, L.S.; Souza Filho, I.R.; Raabe, D.; and Sandim, H.R.Z.; , 'Recrystallization in non-conventional microstructures of 316L stainless steel produced via laser powder-bed fusion: effect of particle coarsening kinetics', *J. Mater. Sci.*, vol. 57, no. 21, pp. 9576–9598, Jun. 2022, doi: 10.1007/s10853-021-06859-1.
[33] T. Voisin, J.B. Forien, A. Perron, S. Aubry, N. Bertin, A. Samanta, A. Baker, Y. M. Wang, New insights on cellular structures strengthening mechanisms and thermal stability of an austenitic stainless steel fabricated by laser powder-bed-fusion, Acta Mater. 203 (Jan. 2021) 116476, https://doi.org/10.1016/J.ACTAMAT.2020.11.018.
[34] E. de Sonis, S. Dépinoy, P.F. Giroux, H. Maskrot, L. Lemarquis, O. Hercher, F. Villaret, A.F. Gourgues-Lorenzon, Dependency of recrystallization kinetics on the solidification microstructure of 316L stainless steel processed by laser powder bed fusion (LPBF), Mater Charact 194 (Dec. 2022) 112370, https://doi.org/10.1016/J.MATCHAR.2022.112370.
[35] Z. Zhou, J. Lv, M. Gui, W. Yang, Strain induced grain growth behavior in laser powder bed fusion fabricated austenitic stainless steel 316L investigated by quasi–in–situ EBSD, Mater. Lett. 376 (Dec. 2024) 137327, https://doi.org/10.1016/J.MATLET.2024.137327.
[36] C. Zhang; Ahmed, S.; Nadimpalli, V.K.; Yu, T.; and Juul Jensen, D.; , 'Recrystallization kinetics in 3D printed 316L stainless steel', *IOP Conf. Ser. Mater. Sci. Eng.*, vol. 1310, no. 1, p. 012042, Aug. 2024, doi: 10.1088/1757-899X/1310/1/012042.
[37] Z. Abbasi, H.R. Abedi, Dynamic recrystallization behavior of selective laser melted 316L stainless steel, J. Mater. Res. Technol. 27 (Nov. 2023) 6458–6473, https://doi.org/10.1016/j.jmrt.2023.11.120.
[38] T. Philippe, P.W. Voorhees, Ostwald ripening in multicomponent alloys, Acta Mater. 61 (11) (Jun. 2013) 4237–4244, https://doi.org/10.1016/J.ACTAMAT.2013.03.049.
[39] S. Chen, G. Ma, G. Wu, A. Godfrey, T. Huang, X. Huang, Strengthening mechanisms in selective laser melted 316L stainless steel, Mater. Sci. Eng. A 832 (Jan. 2022) 142434, https://doi.org/10.1016/J.MSEA.2021.142434.
[40] P. Deng, M. Song, J. Yang, Q. Pan, S. McAllister, L. Li, B.C. Prorok, X. Lou, On the thermal coarsening and transformation of nanoscale oxide inclusions in 316L stainless steel manufactured by laser powder bed fusion and its influence on impact toughness, Mater. Sci. Eng. A 835 (Feb. 2022) 142690, https://doi.org/10.1016/J.MSEA.2022.142690.
[41] L.S. Aota; Bajaj, P.; Zilnyk, K.D.; Ponge, D.; and Sandim, H.R.Z.; , 'The origin of abnormal grain growth upon thermomechanical processing of laser powder-bed fusion alloys', *Materialia (Oxf).*, vol. 20, p. 101243, Dec. 2021, doi: 10.1016/J.MTLA.2021.101243.
[42] E. Nieto-Valeiras; Haouala, S.; and LLorca, J.; , 'On the effect of slip transfer at grain boundaries on the strength of FCC polycrystals', *European Journal of Mechanics - A/Solids*, vol. 91, p. 104427, Jan. 2022, doi: 10.1016/J.EUROMECHSOL.2021.104427.
[43] P. Dolzhenko, M. Tikhonova, M. Odnobokova, R. Kaibyshev, A. Belyakov, On grain boundary engineering for a 316L austenitic stainless steel, Metals (basel) 12 (12) (2022) Dec, https://doi.org/10.3390/met12122185.
[44] M. Shamsujjoha; Agnew, S.R.; Fitz-Gerald, J.M.; Moore, W.R.; and Newman, T.A.; , 'High Strength and Ductility of Additively Manufactured 316L Stainless Steel Explained', *Metall. Mater. Trans. A Phys. Metall. Mater. Sci.*, vol. 49, no. 7, pp. 3011–3027, Jul. 2018, doi: 10.1007/s11661-018-4607-2.
[45] R. Douglas, W. Beard, N. Barnard, S. Lee, S. Shao, N. Shamsaei, T. Jones, R. Lancaster, The influence of energy density on the low cycle fatigue behaviour of laser powder bed fused stainless steel 316L, Int. J. Fatigue 181 (Apr. 2024) 108123, https://doi.org/10.1016/J.IJFATIGUE.2023.108123.
[46] A. Trentin, A. Mardoukhi, A. Lambai, P. Pohjanne, E. Huttunen-Saarivirta, Pitting corrosion of austenitic and duplex stainless steels in dilute acids at elevated temperature: effect of electrolyte chemistry and material microstructure, Corros. Sci. 247 (May 2025) 112769, https://doi.org/10.1016/J.CORSCI.2025.112769.
[47] H. Zhang, P. Xue, L.H. Wu, Q.N. Song, D. Wang, B.L. Xiao, Z.Y. Ma, Effect of grain ultra-refinement on corrosion behavior of ultra-high strength high nitrogen stainless steel, Corros. Sci. 174 (Sep. 2020) 108847, https://doi.org/10.1016/J.CORSCI.2020.108847.
[48] M.H. Ghoncheh, A. Shahriari, N. Birbilis, M. Mohammadi, Process-microstructure-corrosion of additively manufactured steels: a review, Crit. Rev. Solid State Mater. Sci. 49 (4) (Jul. 2024) 607–717, https://doi.org/10.1080/10408436.2023.2255616.
[49] Y. Sun, X. Tan, R. Lan, G. Ran, J. Li, Y. Jiang, Mechanisms of inclusion-induced pitting of stainless steels: a review, J. Mater. Sci. Technol. 168 (Jan. 2024) 143–156, https://doi.org/10.1016/j.jmst.2023.06.008.